LRP 574/97 September 1997

GAE DETECTION FOR MASS MEASUREMENT FOR D-T RATIO CONTROL

J.B. LISTER, L. VILLARD, G. DE RIDDER

CRPP
Centre de Recherches en Physique des Plasmas
Association Euratom - Confédération Suisse

ÉCOLE POLYTECHNIQUE
FÉDÉRALE DE LAUSANNE

Centre de Recherches en Physique des Plasmas (CRPP)
Association Euratom - Confédération Suisse
Ecole Polytechnique Fédérale de Lausanne
PPB, CH-1015 Lausanne, Switzerland *phone: +41 21 693 34 82 / 7 — fax +41 21 693 51 76*

Centre de Recherches en Physique des Plasmas - Technologie de la Fusion (CRPP-TF)
Association Euratom - Confédération Suisse
Ecole Polytechnique Fédérale de Lausanne
CH-5232 Villigen-PSI, Switzerland *phone: +41 56 310 32 59 — fax +41 56 310 37 29*

LRP 574/97 September 1997

GAE DETECTION FOR MASS MEASUREMENT FOR D-T RATIO CONTROL

J.B. LISTER, L. VILLARD, G. DE RIDDER

i) MEASUREMENT OF THE EFFECTIVE PLASMA ION MASS IN LARGE TOKAMAKS USING GLOBAL ALFVEN EIGENMODES

J.B. LISTER, L. VILLARD, G. DE RIDDER

ii) GAE DETECTION FOR MASS MEASUREMENT FOR PLASMA DENSITY CONTROL

JET ARTICLE 14 CONTRACT 950104

J.B. LISTER, L. VILLARD, G. DE RIDDER

MEASUREMENT OF THE EFFECTIVE PLASMA ION MASS IN LARGE TOKAMAKS USING GLOBAL ALFVEN EIGENMODES

J.B. Lister, L. Villard and G. de Ridder

Centre de Recherches en Physique des Plasmas
Association Euratom - Confédération Suisse
Ecole Polytechnique Fédérale de Lausanne
CH-1015 Lausanne, Switzerland

Abstract

The ratio in the centre of a tokamak plasma. One of the simpler measurements put forward in the past is the interpretation of the MHD spectrum in the frequency range of the Global Alfvén Eigenmodes (GAE). However, the frequencies of these modes do not depend only on the plasma mass, but are also quite strongly dependent on the details of the current and density profiles, creating a problem of deconvolution of the estimate of the plasma mass from an implicit relationship between several measurable plasma parameters and the detected eigenmode frequencies.

In view of the lack of competitive diagnostics, this method has been revisited to assess its likely precision for the JET tokamak. Our results show that the low-n GAE modes are sometimes too close to the continuum edge to be detectable and that the interpretation of the GAE spectrum is therefore rendered less direct than had been hoped. However, information on the effective plasma ion mass is still available in the detectable modes and we present a statistical study on the precision with which this quantity could be estimated from the GAE spectrum on JET, including other directly measured or simply available plasma parameters.

1. Introduction

The ratio of deuterium to tritium ions (D-T ratio) should be close to unity in the plasma core to maximise the thermal fusion power. Different sources of deuterium and tritium from neutral beam injection, pellet injection, gas fuelling and recycling from walls and the divertor make the D-T source ratio difficult to estimate. Different radial transport time constants might further confuse the control of the D-T ratio. For these reasons a direct measurement of the D-T ratio is highly desirable. In the absence of a clear candidate for this measurement, we have revisited the use of Global Eigenmodes of the Alfvén Wave (GAE) for determining the core D-T ratio in the JET tokamak.

A method of estimating the effective mass, defined as $A_{eff} = \sum A_i n_i / n_e$ summing over all ion species, was developed on the TCA tokamak [1,2] with a view to measuring either of q(0) or A_{eff}. The method relies on the dispersion relation for Shear Alfvén Waves, given in the cylindrical approximation by:

$$\omega_{nm}^2(r) = \omega^o{}_{nm}^2(r)/A_{eff}(r)[1+\{\omega^o{}_{nm}^2(r)/\omega_{cH}^2\}\{\Sigma n_i(r)A_i^3/n_e(r)Z_i^2\}/A_{eff}(r)^2] \qquad (1)$$

where $\omega^o{}_{nm}^2(r) = B_\phi^2(n+m/q(r))^2/\mu_o n_e(r) m_p R^2$, n and m are the toroidal and poloidal mode numbers, ω_{cH} is the cyclotron frequency of hydrogen and the summation is over all ion species.

The GAE frequencies lie close to but below the minimum of the continuum frequency defined by Equation (1). Many GAE's could be detected using a wide-band frequency sweep and A_{eff} could be estimated from the full spectrum of observed GAE's.

On TCA, about 60 W were launched by a small poloidal emitting antenna. The wavefield of the GAE was detected by broadband magnetic pick-up coils, mixed with the driving frequency to produce amplitude and phase plots of the driven spectrum. This system was used to measure the dynamic behaviour of the effective mass

following the influx of cold H^0 into a D^+ discharge and to feedback control the H-D ratio, both in the TCA tokamak [3].

The GAE spectrum was measured on PETULA using similar techniques to TCA, but the aim of the experiment was to investigate q(0) changes during LHCD sawtooth stabilisation [4]. q(0) measurements were also performed on TEXTOR [5].

The GAEs were launched in all cases using antennae inside the torus. The method has been simple to implement and the GAE spectrum has never been unexpected, even if it can be quite complex, but these results leave us with two open questions. Firstly, we need to assess the likely precision for JET and secondly we need to assess whether the physics of the GAE will be different on a much larger device than TCA, PETULA and TEXTOR. In the remainder of this Paper, we address these questions.

2. Method

The uncertainties in using the GAE frequency as a diagnostic lie in its known sensitivity to the precise details of both the plasma current and density profiles which have considerable experimental uncertainty. The value of the Shear Alfvén Wave continuum frequency on axis $\omega_A(0)$ is a local quantity, determined by the electron density $n_e(0)$ and the safety factor q(0) as well as the effective ion mass $A_{eff}(0)$. In principle $n_e(0)$ and q(0) are knowable. Together with $B_\phi(0)$ and the major radius, we obtain the Shear Alfvén Wave continuum frequency on axis. However, the separation between $\omega_A(0)$ and the eigenmode frequency ω_{GAE} is not a locally-defined quantity and we must infer the value of this separation from the experimental data available. We shall examine the extent to which the usually measured quantities allow us to estimate this separation.

In order to make these assessments, we embarked on a Monte-Carlo based approach to this proposed diagnostic. The purpose was to simulate as closely as possible the likely plasma parameters and determine whether the diagnostic can in

fact "reconstruct" the effective ion mass from simulated experimental (but noiseless) data. Executing this approach required several steps:

- determination of a suitable plasma profile parametrisation
- determination of the realistic parameter ranges
- determination of inter-parameter correlations providing additional constraints
- generation of a large volume of Monte-Carlo plasma parameters
- adjustment of the multi-dimensional parameter space population to simulate a realistic distribution
- generation of a small subset of Monte-Carlo data on the basis of this final distribution, creating 150 plasmas to be analyzed.

Table 1 Definition and range of the plasma parameters

Parameter	Definition	Range
B	toroidal magnetic field	[1-4] T
R	major radius	[2.9-3.0] m
a	minor radius	[1.1-1.3] m
Ip	toroidal plasma current	[1.0-4.5] MA
ne0	total electon density	$[0.5\text{-}8.0]*10^{19}m^{-3}$
nei0	Impurity electron density	[0.-0.25]*ne0
d_con	deuterium concentration	[0-1]
Zimp	Z of impurity	[2-8]
k_j	current parametrization	[1.0-3.0]
b_j	current parametrization	[0.6-1.0]
k_n	density parametrization	[0.3-2]
b_n	density parametrization	[0.7-1.0]

The list of parameters in Table 1 enters in the parametrisation of the problem. The

current density radial profile is parametrised as:

$$j(r) = j_0\left(1 - b\_j\left(\frac{r}{a}\right)^2\right)^{k\_j} \qquad (2)$$

and the different density profiles are similarly parametrised as :

$$n(r) = \tilde{n}\left(1 - b\_n\left(\frac{r}{a}\right)^2\right)^{k\_n} \qquad (3)$$

where $\tilde{n}$ is the total density on the magnetic axis of either ne, ni, nd (deuterium concentration) or nt (tritium concentration). The ranges of values for all these parameters were chosen from a rather small database containing 20 JET discharges.

Considering the large number of parameters to be varied when defining our runs and the impossibility of scanning them systematically, we chose to produce them randomly in the range of values defined by Table 1 to fill the variables space in a way which best approximates the highest performance JET plasmas to be diagnosed. We took care of constraints on various parameters either defined by the range of single parameters or by 2-D correlations such as between I_p and n_e. The following list gives the tests to which our parameters were submitted:

$2.2 < q_{edge} < 5.0$

$0.75 < qaxis < 1.25$

$0.7 < li < 1.1$

$Ip(0.9a)/Ip(a) > 0.9$

$ne0(a)/ne0(0) < 0.25$

$3.0\ 10^{12} < ne0*a*b/Ip < 1.0\ 10^{14}$

The resulting "representative" JET discharges were then simulated in the 1-D ISMENE code [6] to calculate the GAE frequency for modes n = -1...-7 and m = -1. ISMENE considers a cold, magnetized, current carrying, bounded plasma, including

several ion species and various mass and current density profiles. If we suppose small amplitude perturbations, the plasma motion can be modelled by the linearized MHD equations including the Hall term in Ohm's law. We adopt a cylindical geometry and assume that the equilibrium quantities are functions of the radius r only. As usual, we take the time and space dependence of the perturbation quantities as $\exp[i(kz+m\vartheta-\omega t]$, where k and m are the axial and azimuthal wavenumbers. Combining this with Maxwell's equations and after a first order development in $B_{0\vartheta}/B_{0z}$, we can rewrite the wave equation in terms of the perturbed electric and magnetic field $E_\perp$ and $B_{//}$

$$\begin{cases} A\dfrac{1}{r}\dfrac{d}{dr}(rE_\perp) = Gk_\perp E_\perp + \left(A-k_\perp^2\right)i\omega B_{//} \\ \\ A\dfrac{d}{dr}(i\omega B_{//}) = \left(G^2-A^2\right)E_\perp - Gk_\perp i\omega B_{//} \end{cases} \tag{4}$$

where : $$A = \varepsilon_{nn} - k_{//}^2 \tag{5}$$

$$G = i\varepsilon_{n\perp} - 2k_{//}\, B_{0\vartheta}/B_{0z} \tag{6}$$

$$\varepsilon_{nn} = \left(\frac{\omega}{c}\right)^2 S = \left(\frac{\omega}{v_A}\right)^2 \sum_i \frac{f_i}{1-\left(\omega/\omega_{ci}\right)^2} \tag{7}$$

$$\varepsilon_{n\perp} = \left(\frac{\omega}{c}\right)^2 iD = i\left(\frac{\omega}{v_A}\right)^2 \sum_i \frac{f_i\left(\omega/\omega_{ci}\right)}{1-\left(\omega/\omega_{ci}\right)^2} \tag{8}$$

$$k_{//} = \left(kB_{0z} + \frac{m}{r}B_{0\vartheta}\right)\Big/ B_0 \tag{9}$$

$$k_\perp = \left(\frac{m}{r}B_{0z} - kB_{0\vartheta}\right)\Big/ B_0 \tag{10}$$

$$v_A{}^2 = \frac{B_0^2}{\mu_0 \sum_j n_j m_j} \qquad f_i = \frac{n_i m_i}{\sum n_j m_j} \tag{11}$$

n_i and m_i are the density and the mass of the ion species i, $\omega_{ci} = eB_0/m_i$ is the ion cyclotron frequency. f_i represents the fraction of the total ion mass for the species i. The local coordinate system $(r,\perp,//)$ is defined by:

$$\hat{r}, \hat{e}_\perp = \hat{e}_{||} \times \hat{r} \text{ and } \hat{e}_{||} = \mathbf{B}_0/B_0.$$

The Alfvén continuum is defined by A = 0. Assuming $\frac{\omega}{\omega_{ci}} \langle\langle 1$, the second order expansion of A = 0 in ω/ω_{ci} leads to the dispersion relation for the Alfvén continuum, Equation (1).

The ISMENE code needs 3 seconds CPU time on a CRAY-YMP for a single run. All 150 plasmas were analysed in this way giving 1050 eigenfrequencies. Full details of the results are to be found in [7].

3. Results

A first inspection of the raw results was disappointing due to the large number of gaps in the results where the code had failed to locate a GAE peak in the plasma response. Figure 1 shows the proportion of the 150 runs producing a separated GAE resonance, again as a function of toroidal mode number. Of all the 1050 cases run, 445 do not have a distinguishable GAE, a fraction of 42%. The intermediate values n = -2, -3, -4 only show a GAE for 30% of the runs whereas n = -1 and n = -7 show a GAE for over 50% and 90% respectively of the runs.

The values of $\delta\omega/\omega$ are histogrammed as a function of n in Fig. 2, showing a significant variation between different values of n. The maximum gap varies from 12% for n = -1 to 10% for n = -7, with a minimum of 6% for n = -3. The minimum observed gap was 0.28% which represents a limit of detectability. A gap of 10% is exceeded in only 5 cases for n = -1 and 3 cases for n = 7. 98% of cases run had the continuum minimum on axis with only 12 cases for n = -1, and one each for n = -2, n = -3 being off-axis.

Figure 3 shows the percentage GAE separation as a function of the toroidal mode number, for three representative cases of which the values of the input parameters are given in Table 2.

Table 2 : Range of parameters for three representative cases

Parameter	RUN # 1	RUN # 12	RUN # 14
B [T]	3.1858	1.9790	1.4859
R [m]	2.9721	2.9451	2.9958
a [m]	1.2220	1.2232	1.2317
Ip [MA]	3.3147	2.2424	1.4218
n_d [10^{19} m-3]	6.2117	2.4715	1.4487
n_t [10^{19} m-3]	0.3633	1.0871	0.5938
n_imp [10^{19} m-3]	0.1952	0.0799	0.0473
Zimp	5	5	7
k_j	2.8942	1.1324	1.8576
b_j	0.6602	0.9439	0.7647
k_n	1.0827	1.0751	1.7452
b_n	0.7965	0.9717	0.9175

Figures 4 (a,b,c) show the results from a frequency scan across the modes n =-1...-7, m = -1 for these three different cases. The vertical bar indicates the continuum edge (ω_{min} = minimum of $\omega_A(r)$) on each plot. The continuum may be at the edge of the plasma or at a local off-axis minimum. The frequency scans are shown over the range f = (0.86 - 1.01) x ω_{min}. The widths and heights of the GAE peaks are defined by the artificial damping term introduced into the cold plasma model and do not correspond to a physically realistic damping.

In the first case (RUN # 1) all the GAE were present. The distance between the GAE and the continuum varied from 10% (n = -1) to 4% (n = -7) with a minimum of

2.5% for n = -3, n = -4. The separation from the continuum is reduced for intermediate n for all cases seen. The consequence of this can be seen in RUN # 12 and RUN #14. In the former case the GAE disappears into the continuum for n = -2, -3, -4 but subsequently reappears. For the latter case the GAE is only visible for n = -6, -7. These observations were confirmed by runs of ISMENE using a 1-D hot model expanded to second order in ion Larmor radius which showed the same disappearance into and reappearance from the continuum.

We have cross-checked a few cases to confirm the cylindrical model, by performing computations with the finite element code LION [8, 9]. The LION model differs from the ISMENE model not only by the finite aspect ratio, but also in the fact that no assumption is made on the ratio $B_{o\,pol}/B_{o\,tor}$, whereas Equations (4) used in ISMENE were obtained via a first-order expansion in $B_{o\,pol}/B_{o\,tor}$.

Finite aspect ratio effects have been checked. The eigenfrequency of the GAE is more affected by toroidicity for low-n than for high n. But even for n = -1 we found the GAE eigenfrequency changed by less than 3%. Finite aspect ratio also leads to continuum damping of the GAEs through toroidal coupling of shear Alfvén resonance surfaces with different poloidal mode numbers. One can expect that some of the GAEs visible in cylindrical geometry would not be visible in JET because the additional damping broadens and flattens the response peaks.

The proper modelling of $B_{o\,pol}/B_{o\,tor}$ in LION has some more dramatic effects, in particular for the lowest frequency modes and low-n modes. Indeed, the first order approximation in $B_{o\,pol}/B_{o\,tor}$ is not valid for $\omega/\omega_{ci} \rightarrow 0$ or for n = 0. It can be shown that analytically in simple cases (e.g. n = 0, q = const, $\omega/\omega_{ci} \rightarrow 0$) that the first order model predicts existence of GAEs whereas the exact model predicts no GAE. We have checked the most sensitive cases of the database, low-n, low ω/ω_{ci}, Table 3.

Table 3: Comparison of first order in $B_{o\,pol}/B_{o\,tor}$ (ISMENE) with the exact model (LION) for some of the most sensitive cases

NRUN	$\Delta f/f$ [%] (ISMENE)	$\Delta f/f$ [%] (LION)
1	10.14	3.94
86	6.28	5.64
105	11.2	0.78

The relatively high fraction (50%) of n = -1 cases with GAEs as predicted by ISMENE might therefore be exaggerated by the artifact of the first order expansion in $B_{o\,pol}/B_{o\,tor}$.

The first point to note is that we have still found a smaller fraction of identifiable GAE resonances than initially hoped on the basis of TCA experimental results. The underlying reason is that TCA operated with significant values of the GAE frequency compared with the ion cyclotron frequency ω_A/ω_{ci} ~20-30% for n=2. On the other hand the physical size of JET implies ω_A/ω_{ci} only of the order of a few percent for n=2. Since the terms ω/ω_{ci} push the GAE below the continuum, adding to the separation due to field line curvature effects, the separation between the GAE and the continuum in JET is significantly reduced. ITER would have an even smaller value of ω_A/ω_{ci} for a given n.

Moreover, the smaller aspect ratio and larger elongation of JET, compared with TCA, increases the toroidal and elliptical coupling of the GAE to Alfvén resonant surfaces of different poloidal mode numbers, thereby increasing the continuum damping of GAEs [8,9]. The response is broadened and flattened and detection of GAEs in JET would almost certainly be more difficult than in TCA.

The ISMENE results were therefore confirmed as reasonable, provided the probably spurious reappearance of low-n modes is ignored.

4. Analysis

As a first interpretative step, we fit an MLP Neural Network Multi-Layer Perceptron to the mapping {plasma parameters : $\delta\omega/\omega$}, where the plasma parameters are: [k-j, b-j, k-n, b-n, q*], q* being the cylindrical equivalent (Ip R/a^2 B). The MLP provides a generalised functional fitting of an {input:output} multi-dimensional mapping [10]. The values of $\delta\omega/\omega$ for n = -6 and n = -7 are plotted against each other in Fig. 5, showing a high correlation. This implies that the data are systematic but also implies that little additional information can be obtained by using two adjacent eigenmodes. The subsequent MLP analysis was performed for n = -7.

The root mean square residual for the full data is ~ 14.8%. This means that $\delta\omega/\omega$ is predictable to 14.8% of its maximum range of 11%, i.e. a statistical precision in ω of 1.6%.The root mean square residual of the actual values of $\delta\omega/\omega$ is 21% of the full range, namely 2.4%. The MLP prediction has therefore only reduced the uncertainty in $\delta\omega/\omega$ by a factor of 1.5.

A first estimation of A_{eff} can be obtained from

$$A^{o}_{eff} = \left[\frac{B\phi\,(n + m/q^{o})}{R\,\omega_A}\right]^2 \bullet \frac{1}{\mu_o\, n_e(0)\, m_p}$$

in which we assume that $n_e(0)$ is experimentally available and we assume $q^o = 1.0$. The resulting value of A^{o}_{eff} can be fitted by linear regression to the known $A_{eff}(0)$ with the coefficients :

$$\hat{A_{eff}}(0) = 0.545 + 0.715\, A^{o}_{eff}.$$

The relationship between $A_{eff}(0)$ and the estimated $\hat{A_{eff}}(0)$ has an RMS residual of $\sigma = 0.087$. Since the range of $A_{eff}(0)$ is about unity, this corresponds to an RMS residual of 8.7%.

An MLP was fitted to the input variables:

$$li,\ k_n,\ q_{95},\ A^o_{eff}$$

to see to what extent an MLP could reduce the uncertainties. Over the whole dataset for n = -7 the full-scale residual was reduced from 5.6% to 5.1% by varying the number of hidden nodes from 1 to 4, illustrating the lack of improvement.

We conclude that the MLP fit to the input data only reduces the uncertainty by a factor of 1.3. We estimate the uncertainty of $A_{eff}(0)$ as being of the order of 7% for the GAE mode n = -7, m = -1, chosen since it was observed for 140 out of 150 test runs.

We are therefore obliged to draw the conclusion that even if the GAE frequency has a smooth dependence on the individual parameters defining the plasma profiles, the multi-dimensional dependence is not as smooth as had been assumed and hoped. Such a result is the fruit of the Monte-Carlo approach which confronts us in a more direct way with the full problem.

4. Conclusions

1050 JET discharges with different parameters, judiciously chosen, were analysed using a 1-D code. Some cases were benchmarked against a 2-D code. Discrepancies for low-n and low frequencies were noted which could explain why ISMENE finds low-n GAE even when mid-range-n are not resonant. We must be careful interpreting low-n and low frequency results.

The continuum-GAE separation can be predicted rather inaccurately, typically to 15% of its full range. However, this is an uncertainty in the unknown correction to the GAE frequency. The impact on the precision of the effective mass is estimated to be of the order of 7%.

The conclusions of this work can therefore be summarised as follows:

- low-n GAE are probably not excited with a detectable amplitude.
- low frequency, i.e. low (ω/ω_{ci}), low-n GAE are badly modelled by a 1st order model in $B_{o\ pol}/B_{o\ tor}$.
- using low and high n combinations of the GAE to extract q(0) is probably not practicable
- using high-n (-5... -7) GAE would lead to an imprecision of 7% in the experimental estimate of A_{eff}.

ACKNOWLEDGEMENTS

The authors would like to thank the JET staff for their interest and contributions, especially J. How as contract coordinator and D.J. Campbell, B. Schunke and A. Tanga. The work was partly supported by JET Article 14 Contract No 950104 and partly by the Fonds national suisse de la recherche scientifique.

FIGURE CAPTIONS

Fig. 1 Fraction of GAEs found in 150 test runs, as a function of the toroidal mode number.

Fig. 2 Spread of $\delta\omega/\omega$ for different toroidal mode numbers.

Fig. 3 GAE separation as a function of toroidal mode number for the 3 test cases. The solid line is case No 1, the dashed line is case No 14 and the dot-dashed line is case No 12.

Fig. 4(a) Spectral scan over the test case # 1 listed in Table 2.

Fig. 4(b) Spectral scan over the test case # 12 listed in Table 2.

Fig. 4(c) Spectral scan over the test case # 14 listed in Table 2.

Fig. 5 Correlation between the $\delta\omega/\omega$ [%] obtained for n = -6 and n = -7 GAE.

REFERENCES

[1] G.A. Collins, A.A. Howling, J.B. Lister, Ph. Marmillod, Plasma Phys. and Contr. Fusion **29**, 323 (1987)

[2] T. Dudok de Wit, J.B. Lister, B.P. Duval, B. Joye, Ph. Marmillod, Nucl. Fusion **30**, 1493 (1990)

[3] T. Dudok de Wit, B.P. Duval, B. Joye, J.B. Lister, Nucl. Fusion **32**, 359 (1991)

[4] G.A. Collins, A.A. Howling, J.B. Lister, Ph. Marmillod, C. Gormezano, F. Parlange, J.-V. Vallet, D. Van Houtte, Plasma Phys. and Contr. Fusion **29**, 1631 (1987)

[5] P. Descamps, G. Van Wassehove, R. Koch, A.M. Messiaen, P. E. Vandenplas, J.B. Lister, Ph. Marmillod, Phys. Lett. A, **143**, 311 (1990)

[6] K. Appert and J. Vaclavik, in Plasma Physics **24**, 551 (1983)

[7] J.B. Lister, L. Villard, G. de Ridder "GAE detection for mass measurement for D-T ratio control", LRP 574/97 (1997)

[8] L. Villard, K. Appert, R. Gruber, and J. Vaclavik, Comput. Phys. Rep **4**, 95 (1986)

[9] L. Villard, S. Brunner, J. Vaclavik, Nucl. Fusion **35**, 1173 (1995)

[10] J.B. Lister, H. Schnurrenberger, Ph. Marmillod, LRP 398/90 (1990)

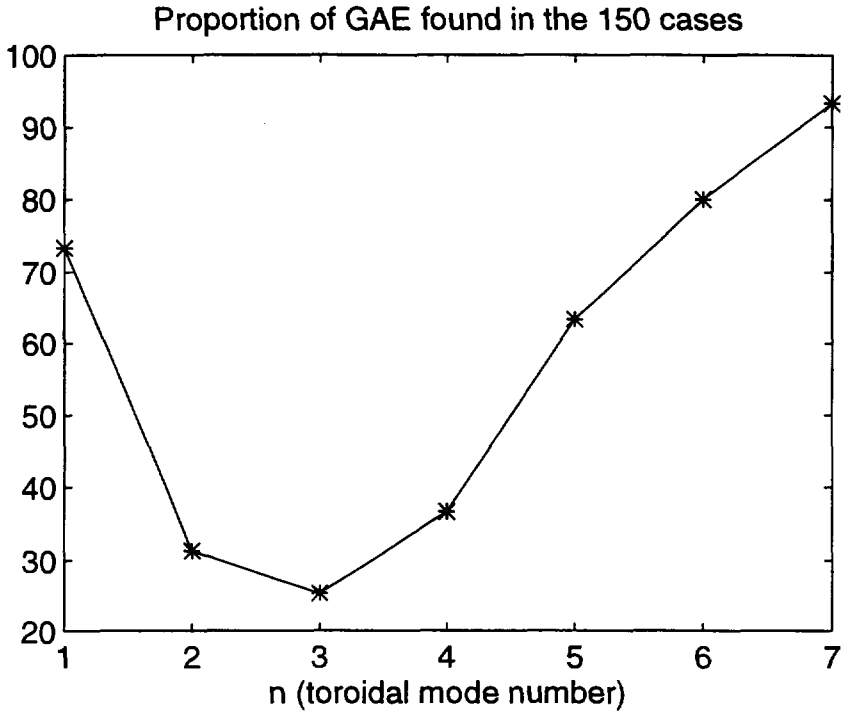

GAE_PROP : 10-Feb-97

Figure 1 *Fraction of GAEs found in 150 test runs, as a function of the toroidal mode number.*

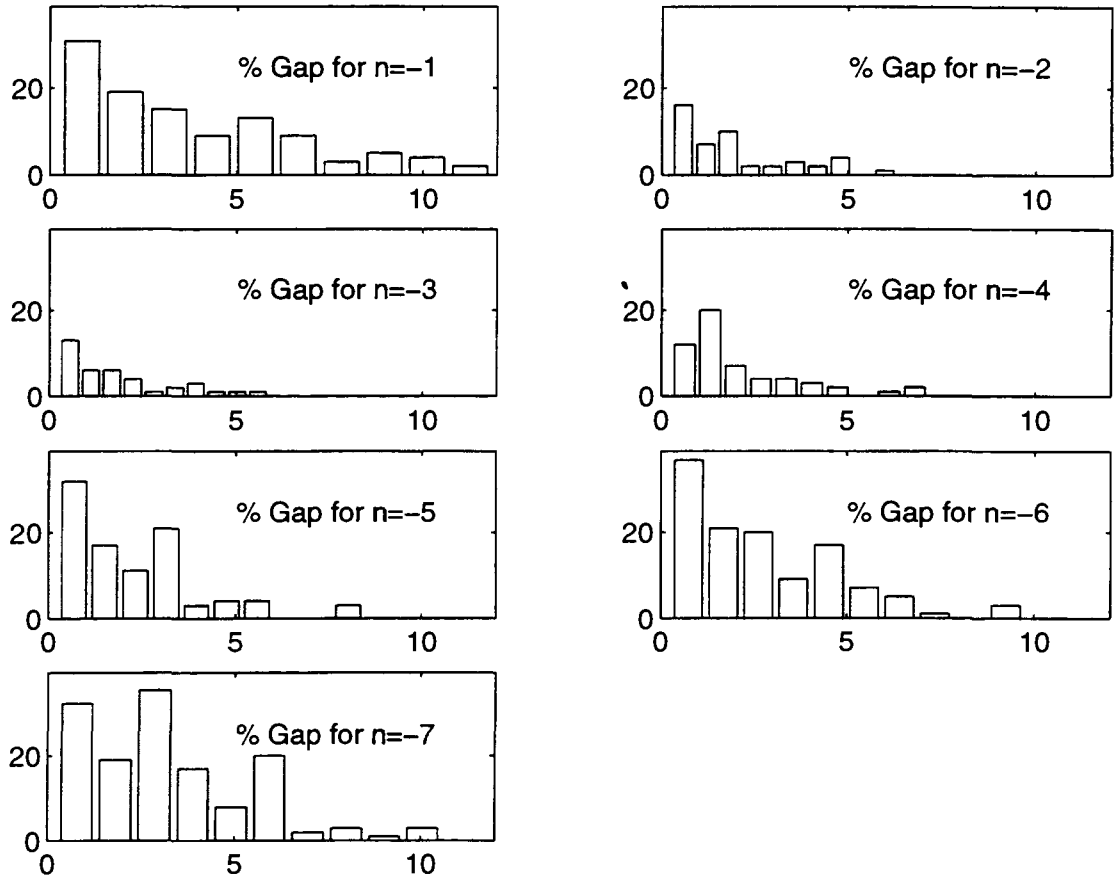

Figure 2. *Spread of $\delta\omega/\omega$ for different toroidal mode numbers.*

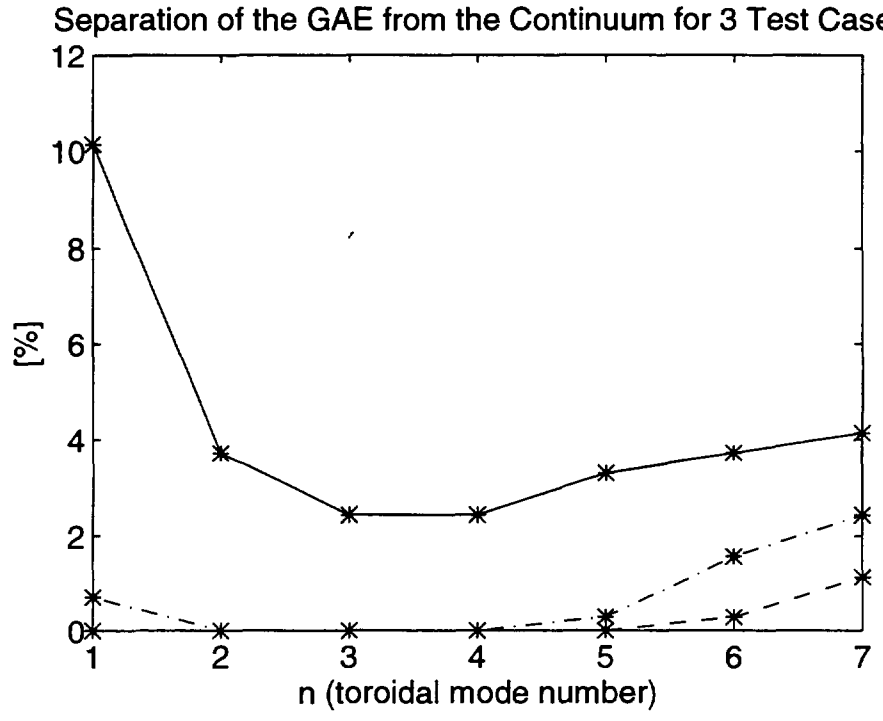

Figure 3. *GAE separation as a function of toroidal mode number for the 3 test cases. The solid line is case #1, the dashed line is case # 13 and the dot-dashed line is case # 12.*

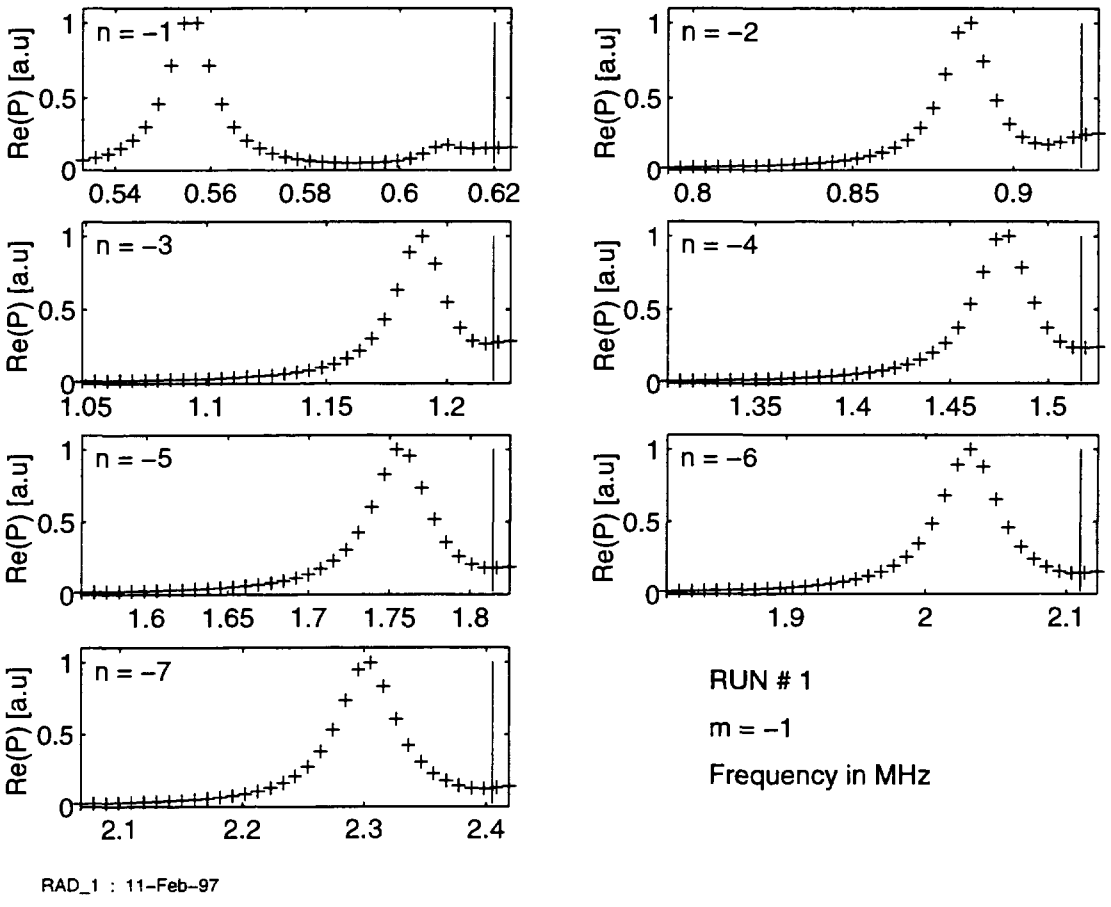

Figure 4(a) *Spectral scan of the case #1 listed in Table 2.*

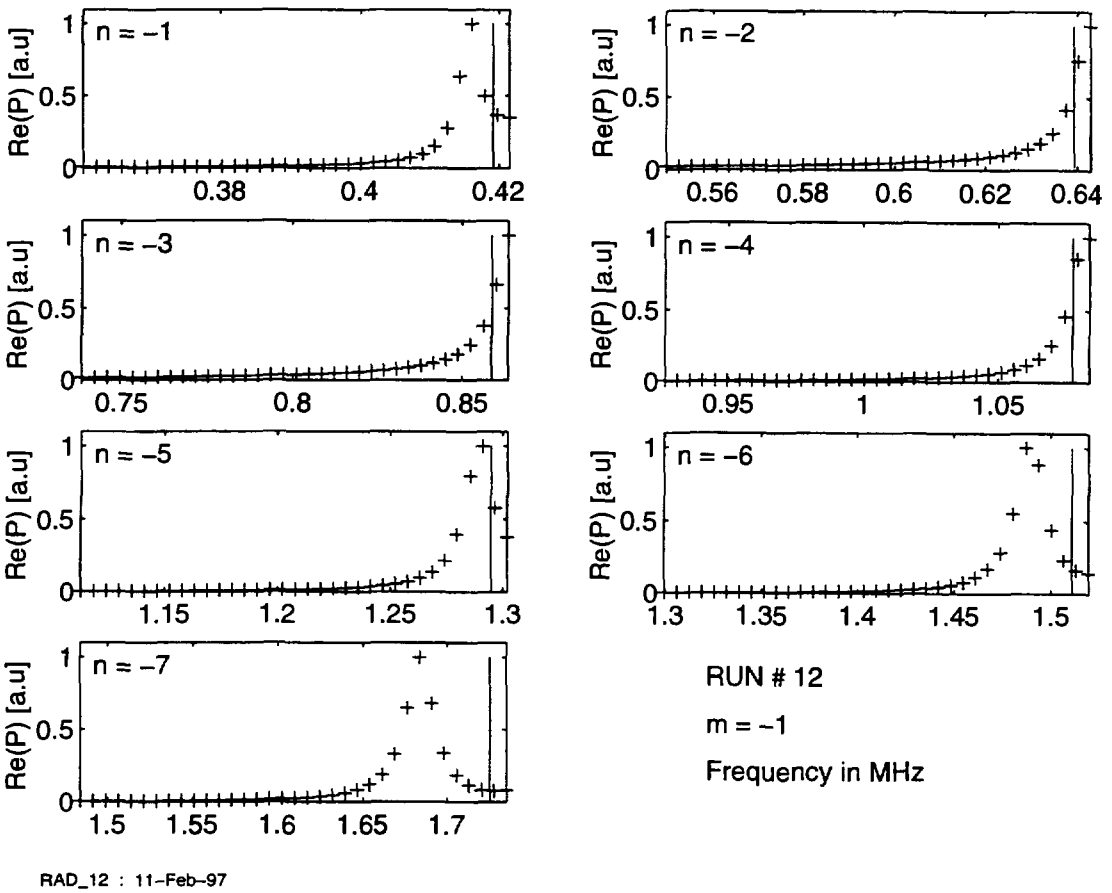

Figure 4(b) *Spectral scan of the case #12 listed in Table 2.*

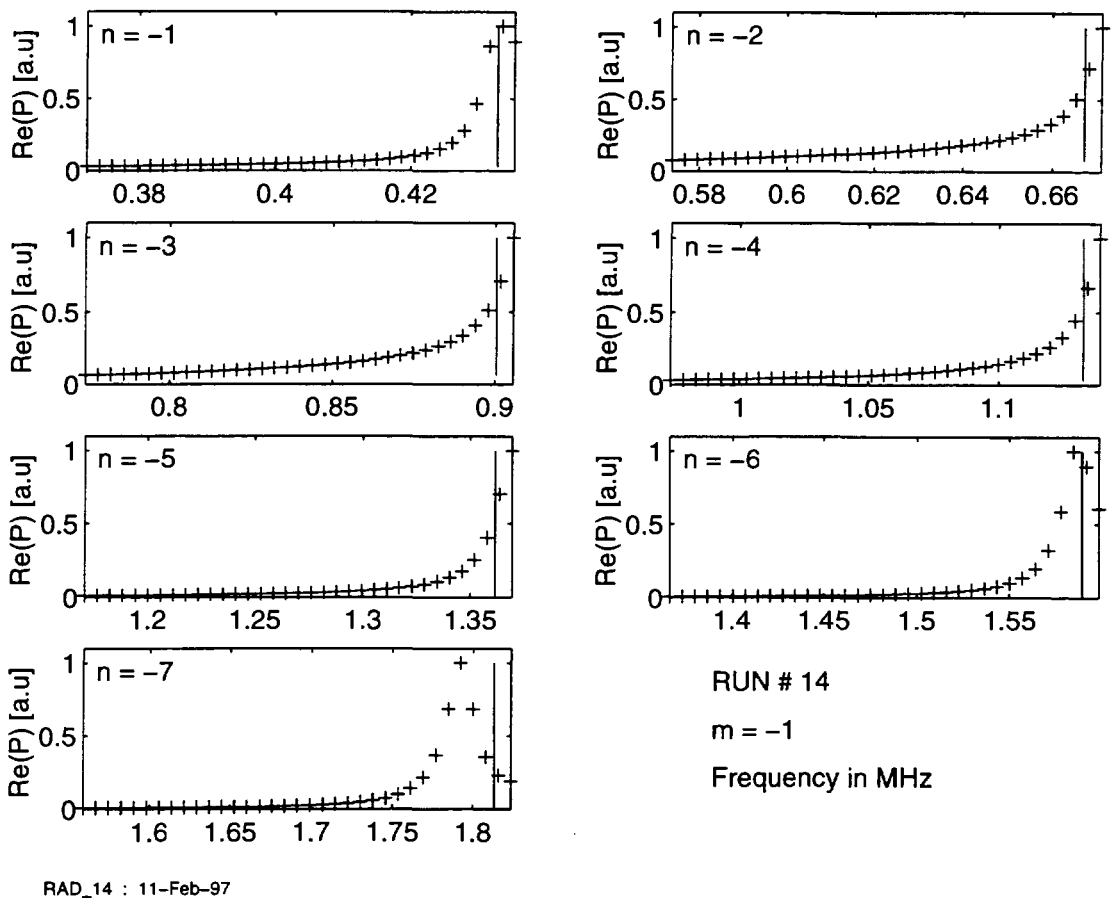

Figure 4(c) *Spectral scan of the case #14 listed in Table 2.*

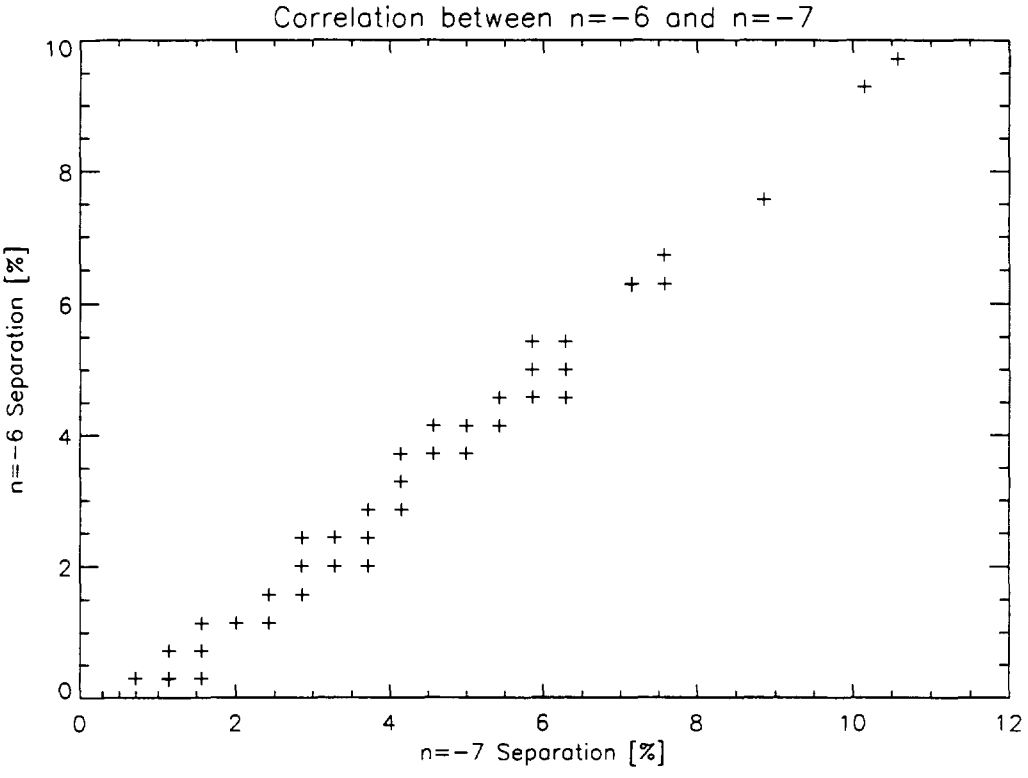

Figure 5. *Correlation between the $\delta\omega/\omega$ [%] obtained for n = -6 and n = -7 GAEs.*

Final Report

JET ARTICLE 14 CONTRACT NO 950104

GAE Detection for Mass Measurement for Plasma Density Control

J.B. LISTER, G. DE RIDDER, L. VILLARD

Centre de Recherches en Physique des Plasmas
Association EURATOM - Confédération Suisse
Ecole Polytechnique Fédérale de Lausanne
CH-1015 LAUSANNE, Switzerland

March 1997

SUMMARY

In view of the interest in obtaining a direct mass measurement in JET D-T plasmas, ultimately for D/T ratio control, the CRPP has performed numerical simulation work to verify the underlying method. The work undertaken is described and the conclusions are presented.

The use of the GAE in JET is concluded to be less interesting than initially hoped. The reasons are discussed. Such a method might, however, provide useful additional information.

CONTENTS

Section 1 outlines the method and describes the approach taken.

Section 2 summarises the theoretical background and introduces the code used in the simulation work.

Section 3 describes the work carried out in generating the simulation data.

Section 4 is an appreciation of the raw results and presents their analysis.

Section 5 concludes the Report.

Annex 1 describes the Multi-Layer Perceptron as used.

Annex 2 tabulates the results of the numerical simulations.

Annex 3 is the JET Article 14 Contract specification.

1. OVERVIEW

The background to this Contract is described in the Article 14 contract proposal in Annex 3, together with a bibliography of previous modelling and experimental work. Previous modelling had indicated that the Global Alfvén Eigenmode (GAE), also referred to in the literature as the Discrete Alfvén Wave (DAW), could be used to determine the plasma effection ion mass, A_{eff}, from the GAE resonance frequencies taken in conjunction with other known or assumed plasma parameters.

The uncertainties in using the GAE frequency as a diagnostic lie in its known sensitivity to the precise details of both the plasma current and density profiles which have considerable experimental uncertainty. The value of the Shear Alfvén continuum frequency on axis, $\omega_A(0)$, is a local quantity, determined by the electron density $n_e(0)$ and the safety factor $q(0)$ as well as the effective ion mass $A_{eff}(0)$. In principle $n_e(0)$ and $q(0)$ are knowable. Together with $B_\phi(0)$ and the major radius, we obtain the Shear Alfvén Wave continuum frequency on axis. However, the separation between $\omega_A(0)$ and the eigenmode frequency ω_{GAE} is not a locally-defined quantity and we must infer the value of this separation from the experimental data available. We shall examine the extent to which the usually measured quantities allow us to estimate this separation.

In order to verify the previous results, we embarked on a Monte-Carlo based approach to this proposed diagnostic. Such an approach should simulate as closely as possible the likely plasma parameters and determine whether the diagnostic can in fact "reconstruct" the effective ion mass from simulated experimental (but noiseless) data. Executing this approach required several steps:

- determination of a suitable plasma profile parametrisation

- determination of the realistic parameter ranges
- determination of inter-parameter correlations providing additional constraints
- generation of a large volume of Monte-Carlo plasma parameters
- adjustment of the multi-dimensional parameter space population to simulate a realistic distribution
- generation of a small subset of Monte-Carlo data on the basis of this final distribution, creating 150 plasmas to be analyzed.

This Monte Carlo Simulation work is described in detail in Section 3.

The resulting "representative" JET discharges were then simulated in a 1-D code described in detail in Section 2, to calculate the GAE frequency for modes n = -1...-7 and m = -1. Time constraints and previous experimental knowledge excluded the intended m = 0 and m = -2 cases. All 150 plasmas were analysed in this way giving 1050 eigenfrequencies which are defined as non-zero where a GAE was detected. The plasma parameters and resulting frequencies are indicated in Fig. 3.2.1, Fig. 3.2.2 and Tables A.2.1 and A.2.2. The computer-time-consuming part of the exercise was thereby concluded.

A first inspection of the raw results was disappointing due to the large number of gaps in the results where the code had failed to locate a GAE peak in the plasma response. Time and effort was spent confirming this result with a 2-D code, described in Section 3. The results were confirmed as reasonable and explanations for the "missing" modes are given in Section 3.

It was empirically confirmed that the inexistant modes were a continuous case of the variation of $\delta\omega/\omega$ with plasma parameters, by fitting a general non-linear function (MLP) to the {input:output} relationship {plasma-parameters : $\delta\omega/\omega$}. Here

$\delta\omega/\omega$ is the fractional separation of the GAE from the value of ω_A on axis, see Section 2. The Multi Layer Perceptron (MLP) is discussed in detail in Annex 1. The variation of $\delta\omega/\omega$ with n is shown in Section 3 and the results were surpising at first, since on all TCA simulations, $\delta\omega/\omega$ was generally decreasing at high n-numbers. The reappearance of higher-n GAE is, therefore, a new feature.

However, the relatively weak population of the GAE found in the 1-D code is essentially a significant nail in the coffin of the proposed diagnostic, since its applicability is going to be restricted to certain ranges of plasma parameters inside the assumed realistic ranges.

Nonetheless we persevered with the n = -1 case, relatively well populated, but not able to use a complete spectrum of GAE frequencies as additional information. The final attempt at the mapping {experimental-data : A_{eff}} was not very encouraging, Section 4.3, and we retreated to a simpler exercise to represent the mapping {plasma-parameters : GAE-frequency}. Note that this mapping simply emulates the running of the 1-D code. The result of this mapping, using the MLP, is shown in Fig. 4.2.1, 4.2.2 of Section 4 and is disappointing, except for n = -1. Different numbers of "hidden nodes" were tried, controlling the number of adjustable parameters in the MLP representation, and results of the fitted and test data are discussed in Section 4.

The number of runs available for examining one single mode is rather minimal. However the conclusion is unavoidable: the MLP does not yield a good fit to the numerically evaluated frequencies as a function of the input parameters.

This conclusion caused us considerable consternation as well as time and effort were spent worrying about the validity of the data from these runs. The validity of the model used, 1st order in $B_o\theta/B_{oz}$, is discussed in Section 2 and even

if this could be debated, the lack of a smooth mapping does not find an explanation in this discussion.

We are therefore obliged to draw the conclusion that even if the GAE frequency has a smooth dependence on the individual parameters defining the plasma profiles, the multi-dimensional dependence is not as smooth as had been assumed and hoped. Such a result is the fruit of the Monte-Carlo approach which confronts us in a more direct way with the full problem.

Nonetheless, the exercise was continued and the inverse MLP mapping between experimental parameters, including a single GAE mode, and A_{eff} was produced for all n = -1...-7 and the results are presented in Section 4.3. The spread in the A_{eff} derived is of the order of $\pm$ 7% which we consider too inaccurate to be of use inside a real-time mixture control loop.

On the basis of the calculations presented, we cannot, therefore, defend the installation of such a diagnostic as a control method on JET. The quality of the additional information obtained would not justify the investment, in our opinion.

The underlying reason for the ill-behaved variation of the GAE frequency over the range of parameters relevant to JET would seem to merit further attention.

2. THEORY AND CODING

2.1 Theory

We consider the model of a cold, magnetized, current carrying, bounded plasma, including several ion species and various mass and current density profiles.

If we suppose small amplitude perturbations, the plasma motion can be modelled by the linearized MHD equations including the Hall term in Ohm's law. We adopt a cylindical geometry and assume that the equilibrium quantities are functions of the radius r only. As usual, we take the time and space dependence of the perturbation quantities as $\exp[i(kz+m\vartheta-\omega t]$, where k and m are the axial and azimuthal wavenumbers. Combining this with Maxwell's equations and after a first order development in $B_{0\vartheta}/B_{0z}$, we can rewrite the wave equation in terms of the perturbed electric and magnetic field $E_\perp$ and $B_{//}$[2.1.1]:

$$\begin{cases} A\dfrac{1}{r}\dfrac{d}{dr}(rE_\perp) = Gk_\perp E_\perp + \left(A-k_\perp^2\right)i\omega B_{//} \\ \\ A\dfrac{d}{dr}(i\omega B_{//}) = \left(G^2-A^2\right)E_\perp - Gk_\perp i\omega B_{//} \end{cases} \tag{2.1.1}$$

where :

$$A = \varepsilon_{nn} - k_{//}^2 \tag{2.1.2}$$

$$G = i\varepsilon_{n\perp} - 2k_{//}\, B_{0\vartheta}/B_{0z} \tag{2.1.3}$$

$$\varepsilon_{nn} = \left(\frac{\omega}{c}\right)^2 S = \left(\frac{\omega}{v_A}\right)^2 \sum_i \frac{f_i}{1-\left(\omega/\omega_{ci}\right)^2} \tag{2.1.4}$$

$$\varepsilon_{n\perp} = \left(\frac{\omega}{c}\right)^2 iD = i\left(\frac{\omega}{v_A}\right)^2 \sum_i \frac{f_i\left(\omega/\omega_{ci}\right)}{1-\left(\omega/\omega_{ci}\right)^2} \tag{2.1.5}$$

$$k_{//} = \left(kB_{0z} + \frac{m}{r}B_{0\vartheta}\right)\Big/ B_0 \tag{2.1.6}$$

$$k_\perp = \left(\frac{m}{r}B_{0z} - kB_{0\vartheta}\right)\Big/ B_0 \tag{2.1.7}$$

$$v_A{}^2 = \frac{B_0^2}{\mu_0 \sum_j n_j m_j} \qquad f_i = \frac{n_i m_i}{\sum n_j m_j} \tag{2.1.8}$$

n_i and m_i are the density and the mass of the ion species i, $\omega_{ci} = eB_0/m_i$ is the ion cyclotron frequency. f_i represents the fraction of the total ion mass for the species i. The local coordinate system $(r,\perp,//)$ is defined by $(r,\perp,//)$ $\hat{r}$, $\hat{e}_\perp = \hat{e}_{//} \times \hat{r}$ and $\hat{e}_{//} = \mathbf{B}_0/B_0$.

The Alfvén continuum is defined by A = 0. Considering that $\frac{\omega}{\omega_{ci}} \langle\langle 1$, the second order expansion of A = 0 leads to the dispersion relation for the Alfvén continuum :

$$\omega_A^2 = \frac{k_{//}^2 v_A^2}{1 + \frac{k_{//}^2 v_A^2}{\omega_{cH}^2} \sum_i f_i \left(\frac{A_i}{Z_i}\right)^2} \left[1 + 0\left(\left(\frac{\omega}{\omega_{CH}}\right)^4\right)\right] \qquad (2.1.9)$$

For the modelling we use $Z^* = \frac{\sum_i n_i Z_i}{\sum_i n_i}$ and $A^* = \frac{\sum_i n_i A_i}{\sum_i n_i}$. The average ion mass per electron is then $A_{eff} = A^*/Z^*$. Rewriting the definition of the Alfvén speed as $v_A^2 = v_{AH}^2 \frac{1}{A_{eff}}$, where $v_{AH}^2 = \frac{B_0^2}{\mu_0 n_e m_p}$ is the Alfvén speed of an equivalent density hydrogen plasma, Equation (2.1.9) can finally be written as :

$$\omega_A^2 = \frac{k_{//}^2 v_{AH}^2 A_{eff}^{-1}}{1 + v_{AH}^2 \frac{k_{//}^2}{\omega_{CH}^2} A_{eff}^{-2} \sum_i \frac{n_i}{n_e} \frac{A_i^3}{Z_i^2}} \left[1 + O\left(\left(\omega/\omega_{CH}\right)^4\right)\right] \qquad (2.1.10)$$

This definition of the Alfvén continuum frequency will be used throughout the paper.

2.2 Coding

The code used for the determination of the location of the Discrete Alfvén

Wave (DAW) is the ISMENE code [2.2.1], a 1-D code using various types of finite elements (linear, hermite cubic). We ran the code with the cold plasma model in a cylindical geometry, neglecting the electron inertia, and using a 251 interval irregular mesh and cubic basis functions. The code needs 3 seconds CPU time on the CRAY-YMP for a single run. More information about the ISMENE code and the convergence proprieties are contained in Ref. [2.2.1]

3. METHOD

In this section the choice of the parameters, their distribution and some typical results obtained from the code are discussed.

3.1 Choice of parameters

The following list of parameters enters into account in the parametrisation of our problem :

Table 3.1.1 : Definition and range of the plasma parameters

Parameter	Definition	Range
B	toroidal magnetic field	[1-4] T
R	major radius	[2.9-3.0] m
a	minor radius	[1.1-1.3] m
Ip	toroidal plasma current	[1.0-4.5] MA
ne0	total electon density	$[0.5\text{-}8.0]*10^{19}m^{-3}$
nei0	Impurity electron density	[0.-0.25]*ne0
d_con	deuterium concentration	[0-1]
Zimp	Z of impurity	[2-8]
k_j	current parametrization	[1.0-3.0]
b_j	current parametrization	[0.6-1.0]
k_n	density parametrization	[0.3-2]
b_n	density parametrization	[0.7-1.0]

The current density radial profile is parametrised as:

$$j(r) = j_0\left(1 - b\_j\left(\frac{r}{a}\right)^2\right)^{k\_j} \qquad (3.1.1)$$

and the different density profiles are similarly parametrised as :

$$n(r) = \tilde{n}\left(1 - b\_n\left(\frac{r}{a}\right)^2\right)^{k\_n} \qquad (3.1.2)$$

where $\tilde{n}$ is the total density on the magnetic axis of either ne, ni, nd (deuterium concentration) or nt (tritium concentration). The ranges of values for all these parameters were chosen from a rather small database containing 20 JET discharges. The characteristics of these discharges and the distribution of the parameters are given in Fig. 3.1.1 (histogrammed).

3.2 Distribution of the Parameters

Considering the large number of parameters to be varied when defining our runs and the impossibility of scanning them systematically, we chose to produce them randomly in the range of values defined by Table 3.1.1 to fill the variables space in a way which best approximates the highest performance JET plasmas to be diagnosed. We took care of constraints on various parameters either defined by the range of single parameters or by 2-D correlations such as between I_p and n_e. The following list gives the total of the tests to which our parameters were submitted:

1) $2.2 < q_{edge} < 5.0$
2) $0.75 < qaxis < 1.25$
3) $0.7 < li < 1.1$
4) $Ip(0.9a)/Ip(a) > 0.9$
5) $ne0(a)/ne0(0) < 0.25$

6) $3.0\ 10^{12} < ne0*a*b/Ip < 1.0\ 10^{14}$

where li is the plasma inductance. In Fig. 3.2.1 we show the distribution of the set of parameters used. The comparison with the JET database is not easy to do because of the smaller quantity of valid shots (70) in comparison to the number of cases run (150) for each toroidal mode number. Nevertheless, we can say that it was very difficult to produce enough cases where li was lower than unity. The full data used for the 150 runs are listed in Table A.2.1.

3.3 Representative Results

In the following sub-section we present some representative results from the 1-D ISMENE code. The values of the input parameters for these three cases are given by Table 3.3.1.

Table 3.3.1 : Range of parameters for three representative cases

Parameter	RUN # 1	RUN # 12	RUN # 14
B [T]	3.1858	1.9790	1.4859
R [m]	2.9721	2.9451	2.9958
a [m]	1.2220	1.2232	1.2317
Ip [MA]	3.3147	2.2424	1.4218
n_d [10^{19} m-3]	6.2117	2.4715	1.4487
n_t [10^{19} m-3]	0.3633	1.0871	0.5938
n_imp [10^{19} m-3]	0.1952	0.0799	0.0473
Zimp	5	5	7
k_j	2.8942	1.1324	1.8576
b_j	0.6602	0.9439	0.7647
k_n	1.0827	1.0751	1.7452
b_n	0.7965	0.9717	0.9175

Figures 3.3.1 (a,b,c) show the results from a frequency scan across the modes n =-1...-7, m = -1 for three different cases. The vertical bar indicates the continuum

edge (ω_{min} = minimum of $\omega_A(r)$) on each plot. The continuum may be at the edge of the plasma or at a local off-axis minimum. The frequency scans are shown over the range f = (0.86 - 1.01) x ω_{min}.

The widths and heights of the GAE peaks are defined by the artificial damping term introduced into the cold plasma model and do not, therefore, correspond to a physically realistic damping.

In the first case (RUN # 1) all the GAE were present. The distance between the GAE and the continuum varied from 10% (n = -1) to 4% (n = -7) with a minimum of 2.5% for n = -3, n = -4. The separation from the continuum is reduced for intermediate n for all cases seen. The consequence of this can be seen in RUN # 12 and RUN #14. In the former case the GAE disappears into the continuum for n = -2, -3, -4 but subsequently reappears. For the latter case the GAE is only visible for n = -6, -7. These observations were confirmed by runs of ISMENE using a 1-D hot model expanded to second order in ion Larmor radius which showed the same disappearance into and reappearance from the continuum.

3.4 Comparison with 2-D modelling

The 2-D modelling of GAE is not part of the present Article 14 contract. However, we have cross-checked a few cases to confirm the cylindrical model, by performing computations with the finite element code LION [3.5.1, 3.5.2]. The LION model differs from the ISMENE model not only by the finite aspect ratio, but also in the fact that no assumption is made on the ratio $B_{o\,pol}/B_{o\,tor}$, whereas Equations (2.1.1) used in ISMENE have been obtained via a first-order expansion in $B_{o\,pol}/B_{o\,tor}$.

Finite aspect ratio effects have been checked. The eigenfrequency of the GAE is

more affected by toroidicity for low-n than for high n. But even for n = -1 we found the GAE eigenfrequency changed by less than 3%. Finite aspect ratio also leads to continuum damping of the GAEs through toroidal coupling of shear Alfvén resonance surfaces with different poloidal mode numbers. One can expect that some of the GAEs visible in cylindrical geometry would not be visible in JET because the additional damping broadens and flattens the response peaks.

The proper modelling of $B_{o\,pol}/B_{o\,tor}$ in LION has some more dramatic effects, in particular for the lowest frequency modes and low-n modes. Indeed, the first order approximation in $B_{o\,pol}/B_{o\,tor}$ is not valid for $\omega/\omega_{ci} \rightarrow 0$ or for n = 0. It can be shown that analytically in simple cases (e.g. n = 0, q = const, $\omega/\omega_{ci} \rightarrow 0$) that the first order model predicts existence of GAEs whereas the exact model predicts no GAE. We have checked the most sensitive cases of the database (low-n, low ω/ω_{ci} (see Table 3.4.1).

Table 3.4.1: Comparison of first order in $B_{o\,pol}/B_{o\,tor}$ (ISMENE) with the exact model (LION) for some of the most sensitive cases

NRUN	Δf/f [%] (ISMENE)	Δf/f [%] (LION)
1	10.14	3.94
86	6.28	5.64
105	11.2	0.78

The relatively high fraction (50%) of n = -1 cases with GAEs as predicted by ISMENE (See Fig. 3.3.3) might therefore be exagerated by the artifact of the first order expansion in $B_{o\,pol}/B_{o\,tor}$.

3.5 Understanding of the spectrum

The first point to note is that we have found a smaller fraction of identifiable GAE resonances than initially hoped on the basis of TCA experimental results. The underlying reason is that TCA operated with significant values of the GAE frequency compared with the ion cyclotron frequency ω_A/ω_{ci} ~20-30%. On the other hand the physical size of JET implies ω_A/ω_{ci} of the order of a few percent. Since the terms ω/ω_{ci} push the GAE below the continuum, adding to the separation due to field line curvature effects, the separation between the GAE and the continuum in JET is significantly reduced. {ITER would have an even smaller value of ω_A/ω_{ci}.}

Moreover, the smaller aspect ratio and larger elongation of JET (as compared with TCA) increases the toroidal and elliptical coupling of the GAE to Alfvén resonant surfaces of different poloidal mode numbers, thereby increasing the continuum damping of GAEs. The response is broadened and flattened and therefore detection of GAEs in JET is almost certainly more difficult than in TCA.

4. ANALYSIS OF THE RESULTS

4.1 Global Analysis

Table A.2.2 shows the full set of eigenmode frequencies expressed as the percentage gap between the Alfvén Continuum frequency on axis and the GAE frequency itself, referred to as the GAE separation, for all 1050 cases evaluated.

The first remark is that of all the 1050 cases run, 445 do not have a distinguishable GAE, a fraction of 42%. The maximum gap varies from 12% for n = -1 to 10% for n = -7, with a minimum of 6% for n = -3. The minimum observed

gap was 0.28% which represents a limit of detectability. A gap of 10% is exceeded in only 5 cases for n = -1 and 3 cases for n = 7. 98% of cases run had the continuum minimum on axis with only 12 cases for n = -1, and one each for n = -2, n = -3 being off-axis.

Figure 4.1.1 shows the percentage GAE separation as a function of the toroidal mode number, for 3 representative cases studied in Section 3.3. Figure 4.1.2 shows the proportion of the 150 runs producing a separated GAE resonance, again as a function of toroidal mode number.

The values of $\delta\omega/\omega$ are histogrammed as a function of n in Fig. 4.1.3, showing a significant variation between different values of n. The intermediate values n = -2, -3, -4 only show a GAE for 30% of the runs whereas n = -1 and n = -7 show a GAE for over 50% and 90% respectively of the runs. Such a disappearance of the GAE at zero gap for intermediate n was already noted in the detailed inspection of RUNS 1, 12, 14.

4.2. MLP emulation of the 1-D code

As a first interpretative step, we fit an MLP to the mapping {plasma parameters : $\delta\omega/\omega$}, where the plasma parameters are: [k-j, b-j, k-n, b-n, q*], q* being the cylindrical equivalent (Ip R/a^2 B). The MLP was chosen with a varying number of hidden-layer elements and the fit was performed on 50% of the available data. After fitting, the other 50% were used to test the generalisation of the fit. The variation of the RMS full-scale fractional error is shown in Fig. 4.2.1 for 2 cases, n = -1 and n = -7. Both show quite poor values of residual with a reasonable number (3-5) of hidden layer elements, the unseen test data being increasingly bad as the number of degrees of freedom in the fit increases.

Figure 4.2.2 shows the normalised residuals as a function of the normalised target values, during the fitting procedure, for n = -7, and 4 nodes in the MLP hidden layer.

The root mean square residual for the full data is ~ 14.8%. This means that $\delta\omega/\omega$ is predictable to 14.8% of its maximum range of 11%, i.e. a statistical precision in ω of 1.6%.

The root mean square residual of the actual values of $\delta\omega/\omega$ is 21% of the full range, namely 2.4%. The MLP prediction has therefore only reduced the uncertainty in $\delta\omega/\omega$ by a factor of 1.5.

The values of $\delta\omega/\omega$ for n = -6 and n = -7 are plotted against each other in Fig. 4.2.3, showing a high correlation. This implies that the data are systematic but also implies that little additional information can be obtained by using two adjacent eigenmodes.

Other combinations of parameters were tested. Reducing the number of determining parameters all led to an increase in the predictive uncertainty.

4.3 MLP evaluation of A_{eff}

The first estimation of A_{eff} can be obtained from

$$A_{eff}^{o} = \left[\frac{B\phi\,(n + m/q^{o})}{R\,\omega_A}\right]^2 \bullet \frac{1}{\mu_o\, n_e(0)\, m_p}$$

in which we assume that $n_e(0)$ is experimentally available and we assume $q^o = 1.0$. The resulting value of A_{eff}^{o} can be fitted by linear regression to the known $A_{eff}(0)$ with the coefficients :

$$\hat{A}_{eff}(0) = 0.545 + 0.715\, A^{o}_{eff}.$$

The relationship between $A_{eff}(0)$ and the estimated $\hat{A}_{eff}(0)$ is shown in Fig. 4.3.1(a) and has an RMS residual of $\sigma = 0.087$. Since the range of $A_{eff}(0)$ is about unity, this corresponds to an RMS residual of 8.7%.

An MLP was fitted to the input variables:

$$li,\ k_n,\ q_{95},\ A^{o}_{eff}$$

to see to what extent an MLP could reduce the uncertainties. Over the whole dataset for n = -7 the full-scale residual was reduced from 5.6% to 5.1% by varying the number of hidden nodes from 1 to 4, illustrating the lack of improvement. Figure 4.3.1(b) shows the variation for 1 hidden node, which represents a non-linear distortion of a linear combination of the input variables.

We conclude that the MLP fit to the input data only reduces the uncertainty by a factor of 1.3. We estimate the uncertainty of $A_{eff}(0)$ as being of the order of 7% for the GAE mode n = -7, m = -1, chosen since it was observed for 140 out of 150 test runs.

5. CONCLUSIONS

1050 JET discharges with different parameters, judiciously chosen, were analysed using a 1-D code. Some cases were benchmarked against a 2-D code. Discrepancies for low-n and low frequencies were noted which could explain why ISMENE finds low-n GAE even when mid-range-n are not resonant. We must be

careful interpreting low-n and low frequency results.

The continuum-GAE separation can be predicted rather inaccurately, typically to 15% of its full range. However, this is an uncertainty in the unknown correction to the GAE frequency. The impact on the precision of the effective mass is estimated to be of the order of 7%.

The conclusions of this work can therefore be summarised as:

- low-n GAE are probably not excited with a detectable amplitude.
- low frequency (i.e. low (ω/ω_{ci})/low-n GAE are badly modelled with a 1st order model in $B_{o\ pol}/B_{o\ tor}$.
- using low/high n combinations of the GAE to extract q(0) is probably a non-starter, but outside the scope of this contract.
- using high-n (-5... -7) GAE would lead to an imprecision of 7% in the experimental estimate of A_{eff}.

ACKNOWLEDGEMENTS

The authors would like to thank the JET staff for their interest and contributions, especially J. How as contract coordinator and D.J. Campbell, B. Schunke and A. Tanga.

The work was partly supported by JET Article 14 Contract No 950104 and partly by the Fonds national suisse de la recherche scientifique.

FIGURE CAPTIONS

3.1.1(a) Distributions of parameters in the JET database.

3.1.1(b) Distributions of parameters in the JET database.

3.2.1(a) Distributions of the individual parameters chosen to be representative of JET data on a discharge by discharge basis.

3.2.1(b) Distributions of the individual parameters chosen to be representative of JET data on a discharge by discharge basis.

3.2.2(a) Distributions of the individual parameters chosen to be representative of JET data, histogrammed.

3.2.2(b) Distributions of the individual parameters chosen to be representative of JET data, histogrammed.

3.3.1(a) Spectral scan over the test run # 1 listed in Table 3.3.1.

3.3.1(b) Spectral scan over the test run # 12 listed in Table 3.3.1.

3.3.1(c) Spectral scan over the test run # 14 listed in Table 3.3.1.

4.1.1 GAE separation as a function of toroidal mode number for the 3 test cases. The solid line is case No 1, the dashed line is case No 14 and the dot-dashed line is case No 12.

4.1.2 Fraction of GAEs found in 150 test runs, as a function of the toroidal mode number.

4.1.3 Spread of $\delta\omega/\omega$ for different toroidal mode numbers.

4.2.1 RMS residual when fitting GAE separation to the imposed plasma parameters. Crosses are fitted population, open circles are the test population.

4.2.2 Representation of the residuals as a function of the target values for n = -7 and 4 hidden elements.

4.2.3 Correlation between the $\delta\omega/\omega$ [%] obtained for n = -6 and n = -7 GAE.

4.3.1(a) The A_{eff} residuals for a linear fit.

4.3.1(b) The A_{eff} residuals for an MLP fit.

A.2.1. Schematic of the Multi-Layer Perceptron.

REFERENCES

2.1.1 K. Appert and J. Vaclavik, in Plasma Physics **24**, 551, (1983)

2.2.1 Proc. of NUMOP 85. Contributed Papers in Comput. Physics Communications **40** (1) (1986) 1 - 158

3.5.1 Villard, L, Appert, K., Gruber, R., and Vaclavik, J., Comput. Phys. Rep. **4**, 95 (1986)

3.5.2 Villard, L., Brunner, S., Vaclavik, J., Nucl. Fusion **35** (1995) 1173

A.1.1 Lister J., Schnurrenberger H., Marmillod Ph., LRP 398/90 (1990)

ANNEX 1

THE MULTILAYER PERCEPTRON

The MLP is an explicit non-linear and continuous mathematical relationship between a multi-variable input data vector M_i (in our case diagnostic information) and a multi-variable output data vector G_i (in our case ultimately the effective plasma mass). The MLP is often represented schematically as in Fig. A.2.1. The input vector, of dimension N_1, is linearly projected by a matrix $\underline{W}_{12}$ onto a usually reduced intermediate vector of dimension N_2. The size of this intermediate vector is the only design choice when specifying the MLP configuration. The reduced vector is then passed element by element through a compression function S, known as the sigmoidal function, which is bounded ± 1, continuous, differentiable and monotonically increasing. The chosen sigmoidal function is:

$$S(x) = \frac{2}{\left(1+e^{-x}\right)} + 1 \qquad \text{(A.1.1)}$$

The compressed vector is then linearly transformed by a second matrix $\underline{W}_{23}$ into an output vector of dimension N_3. Such a configuration is referred to as a 1-hidden-layer MLP (an MLP-1). If we recompress and re-transform the output vector to produce a new output vector, we have a 2-hidden-layer MLP (an MLP-2) and so on.

The MLP-1 representation of a non-linear map $\hat{G}$ can therefore be written explicitly as

$$\hat{G}(\underline{\mathbf{M}}) = \underline{\mathbf{W}}_{23} \bullet \left[\frac{2}{\left(1+e^{-\underline{\mathbf{W}}_{12} \cdot \underline{\mathbf{M}}}\right)} - 1 \right] \qquad \text{(A.1.2)}$$

The vector exponent denotes an element by element exponentiation, giving a vector result. In practice, a constant term is added to each non-output layer to provide an offset bias.

A wide range of literature can be found on the generality of the MLP-1 and MLP-2 fuctions. It has been demonstrated that all bounded continuous functions can be expressed as an MLP-2 over a given volume in the space of $\underline{\mathbf{M}}$. A similar demonstration has been proposed for the case of the MLP-1. The work in this paper is restricted to MLP-1 mappings which should be adequate for the particular problem.

Having established the applicability of an MLP-1 network, two problems remain:

(i) choosing the size of the condensed hidden vector and

(ii) finding the optimal linear transformation matrices $\mathbf{W}_{12}$ and $\mathbf{W}_{23}$.

The first question is a compromise. Too few elements in the intermediate vector result in a too encoded form of the output, with linearly interdependent output variables. Too many elements lead to a badly defined set of matrices. As the number of free parameters increases, we also risk finding a solution which is adapted to the fitted examples, rather than generalising the functional dependence, the well-known problem of overfitting or bias.

The second question is fully discussed in Ref. [A.1.1]. The aim is to minimise the sum of the squares of the errors between examples of data which have been

modelled, $\underline{G}i = G(Mi)$, and the estimated form of $\hat{G}$ given by the MLP-1 mapping (A.1.2). We define an RMS residual for each output denoted j:

$$\sigma_j = \frac{1}{2}\sqrt{\frac{\sum_i \left[\underline{G}_{ij} - \hat{G}(\underline{M}_i)_j\right]^2}{\text{number of examples}}} \qquad \text{(A.1.3)}$$

In order to restrict the range of the values of the matrices $\underline{W}_{12}$ and $\underline{W}_{23}$, we normalise the vectors $\underline{G}$ and $\underline{M}$ to lie within the cubes $[-1, 1]^{N3}$ and $[-1, 1]^{N1}$ respectively. Expressing A.1.3 for σ_j therefore corresponds to the residual as a fraction of the full-scale range of the j-th parameter (% FS).

In practice, we have minimised the RMS value of σ_j, using only half of the available mapping examples $\{\underline{M}_j, \underline{G}_j\}$. The remaining examples are used to test the general validity of the approximated function. The minimisation is performed using the Generalised Adaptive Recipe [A.1.1], a modification of the standard gradient Descent Technique.

ANNEX 1

THE MULTILAYER PERCEPTRON

The MLP is an explicit non-linear and continuous mathematical relationship between a multi-variable input data vector M_i (in our case diagnostic information) and a multi-variable output data vector G_i (in our case ultimately the effective plasma mass). The MLP is often represented schematically as in Fig. A.2.1. The input vector, of dimension N_1, is linearly projected by a matrix $\underline{W}_{12}$ onto a usually reduced intermediate vector of dimension N_2. The size of this intermediate vector is the only design choice when specifying the MLP configuration. The reduced vector is then passed element by element through a compression function S, known as the sigmoidal function, which is bounded ± 1, continuous, differentiable and monotonically increasing. The chosen sigmoidal function is:

$$S(x) = \frac{2}{\left(1+e^{-x}\right)} + 1 \qquad \text{(A.1.1)}$$

The compressed vector is then linearly transformed by a second matrix $\underline{W}_{23}$ into an output vector of dimension N_3. Such a configuration is referred to as a 1-hidden-layer MLP (an MLP-1). If we recompress and re-transform the output vector to produce a new output vector, we have a 2-hidden-layer MLP (an MLP-2) and so on.

The MLP-1 representation of a non-linear map $\hat{G}$ can therefore be written explicitly as

$$\hat{G}(\underline{M}) = \underline{W}_{23} \bullet \left[\frac{2}{\left(1+e^{-\underline{W}_{12} \cdot \underline{M}}\right)} - 1 \right] \qquad \text{(A.1.2)}$$

The vector exponent denotes an element by element exponentiation, giving a vector result. In practice, a constant term is added to each non-output layer to provide an offset bias.

A wide range of literature can be found on the generality of the MLP-1 and MLP-2 fuctions. It has been demonstrated that all bounded continuous functions can be expressed as an MLP-2 over a given volume in the space of $\underline{\mathbf{M}}$. A similar demonstration has been proposed for the case of the MLP-1. The work in this paper is restricted to MLP-1 mappings which should be adequate for the particular problem.

Having established the applicability of an MLP-1 network, two problems remain:

(i) choosing the size of the condensed hidden vector and

(ii) finding the optimal linear transformation matrices $\mathbf{W}_{12}$ and $\mathbf{W}_{23}$.

The first question is a compromise. Too few elements in the intermediate vector result in a too encoded form of the output, with linearly interdependent output variables. Too many elements lead to a badly defined set of matrices. As the number of free parameters increases, we also risk finding a solution which is adapted to the fitted examples, rather than generalising the functional dependence, the well-known problem of overfitting or bias.

The second question is fully discussed in Ref. [A.1.1]. The aim is to minimise the sum of the squares of the errors between examples of data which have been modelled, $\underline{G}i = G(Mi)$, and the estimated form of $\hat{G}$ given by the MLP-1 mapping (A.1.2). We define an RMS residual for each output denoted j:

$$\sigma_j = \frac{1}{2}\sqrt{\frac{\sum_i \left[\underline{G}_{ij} - \hat{G}(\underline{M}_i)_j\right]^2}{\text{number of examples}}} \qquad \text{(A.1.3)}$$

In order to restrict the range of the values of the matrices $\underline{\mathbf{W}}_{12}$ and $\underline{\mathbf{W}}_{23}$, we normalise the vectors $\underline{G}$ and $\underline{M}$ to lie within the cubes $[-1, 1]^{N3}$ and $[-1, 1]^{N1}$ respectively. Expressing A.1.3 for σ_j therefore corresponds to the residual as a fraction of the full-scale range of the j-th parameter (% FS).

In practice, we have minimised the RMS value of σ_j, using only half of the available mapping examples $\{\underline{M}_j, \underline{G}_j\}$. The remaining examples are used to test the general validity of the approximated function. The minimisation is performed using the Generalised Adaptive Recipe [A.1.1], a modification of the standard gradient Descent Technique.

ANNEX 2 - NUMERICAL SIMULATION DATA

Table A.2.1 Input data for the 150 cases run

Run	Ip	Rmaj	Bphi	Aeff	Ne(0)	Li	q 95	q(0)
1	3.315	2.972	3.186	2.284	7.551	1.045	2.210	0.925
2	2.232	2.973	2.180	2.334	1.472	1.080	2.114	0.911
3	3.753	2.905	3.288	3.185	6.789	1.033	2.068	0.954
4	2.741	2.964	2.776	3.121	4.654	0.911	2.273	1.122
5	2.306	2.993	2.197	3.184	1.246	0.914	2.097	1.139
6	1.341	2.957	1.592	2.651	3.253	1.045	2.799	1.180
7	3.623	2.967	3.375	2.466	4.625	0.865	2.036	1.163
8	2.188	2.905	2.307	2.769	3.227	0.977	2.509	1.189
9	4.179	2.999	3.969	3.276	6.644	0.992	2.050	0.908
10	3.341	2.950	2.886	2.793	3.651	0.871	2.102	1.198
11	2.531	2.907	2.224	2.378	7.216	0.876	2.113	1.138
12	2.242	2.945	1.979	2.561	4.678	0.908	2.052	1.111
13	1.034	2.922	1.055	2.362	4.897	0.858	2.220	1.232
14	1.422	2.996	1.486	2.556	2.374	0.943	2.434	1.191
15	2.529	2.932	2.618	3.050	3.798	0.989	2.259	1.024
16	4.073	2.916	3.476	2.672	7.040	1.061	2.159	0.906
17	3.874	2.916	3.723	2.132	6.482	0.928	2.261	1.109
18	2.985	2.925	3.060	2.849	5.760	1.040	2.173	0.979
19	3.109	2.978	2.997	2.667	5.828	0.963	2.163	1.068
20	2.983	2.908	3.000	2.764	2.852	0.984	2.437	1.108
21	3.100	2.965	3.061	2.544	7.397	0.988	2.108	0.942
22	3.428	2.973	3.382	2.077	7.766	1.015	2.299	0.994
23	3.810	2.987	3.404	2.344	2.068	0.813	2.054	1.235
24	3.788	2.905	3.797	3.084	4.024	0.934	2.276	1.144
25	4.088	2.934	3.661	3.268	7.921	1.019	2.106	0.983
26	3.276	2.997	2.658	3.061	6.537	1.049	2.084	0.904
27	4.119	2.953	3.546	2.255	3.000	1.012	2.052	0.934
28	1.598	2.970	1.602	2.529	6.615	1.017	2.335	1.007
29	1.623	2.913	1.902	2.799	3.519	1.086	2.806	1.166
30	3.837	2.914	3.482	2.338	4.377	0.850	2.135	1.240
31	2.799	2.964	2.997	2.981	5.786	0.938	2.218	1.144
32	2.694	2.905	2.964	2.887	5.950	0.986	2.564	1.243
33	1.465	2.962	1.560	3.203	2.025	1.032	2.362	1.068
34	2.748	2.958	3.403	2.352	1.982	1.063	2.742	1.155
35	2.773	2.920	3.127	3.123	2.884	0.983	2.482	1.204
36	4.470	2.965	3.975	2.710	7.799	0.803	2.055	1.229
37	3.628	2.912	3.725	3.220	1.762	0.950	2.342	1.104
38	3.500	2.930	2.952	3.335	4.656	1.082	2.035	0.827
39	2.503	2.931	2.720	3.006	2.335	0.999	2.426	1.175
40	3.836	2.965	3.582	3.176	5.431	0.902	2.193	1.102
41	1.657	2.954	1.435	2.518	2.957	0.877	2.063	1.172
42	3.194	2.994	3.101	2.819	0.789	0.987	2.263	1.073
43	3.795	2.906	3.162	2.215	7.746	0.906	2.117	1.145
44	3.807	2.933	3.630	2.837	6.864	0.837	2.152	1.224
45	4.253	2.962	3.675	3.065	3.266	0.869	2.191	1.214
46	2.257	2.921	2.353	2.910	1.164	1.049	2.427	1.098
47	1.602	2.950	1.558	2.833	4.646	0.976	2.360	1.126
48	2.504	2.957	2.456	2.312	6.643	0.926	2.288	1.220
49	2.835	2.977	2.668	3.200	6.093	0.899	2.169	1.204
50	2.548	2.941	3.141	2.518	3.254	1.066	2.738	1.221

Run	Ip	Rmaj	Bphi	Aeff	Ne(0)	Li	q 95	q(0)
51	3.331	2.950	3.903	2.436	2.903	1.045	2.471	1.044
52	1.893	2.905	1.517	2.882	7.108	0.841	2.057	1.197
53	2.133	2.925	2.378	3.221	7.498	1.029	2.826	1.212
54	2.944	2.952	3.553	2.553	6.352	1.069	2.663	1.165
55	1.324	2.990	1.083	3.019	3.779	0.900	2.061	1.148
56	2.578	2.925	3.109	3.155	3.504	0.956	2.547	1.248
57	3.387	2.925	3.280	3.010	6.283	0.847	2.230	1.228
58	3.331	2.954	3.662	3.012	7.199	1.061	2.485	1.105
59	2.938	2.917	3.191	2.366	1.870	1.028	2.480	1.111
60	2.099	2.959	2.071	2.772	6.840	1.013	2.385	1.082
61	4.271	2.976	3.751	2.462	6.196	0.836	2.093	1.234
62	3.365	2.986	3.162	2.513	4.831	0.886	2.106	1.146
63	3.791	2.941	3.419	2.718	7.991	0.938	2.011	1.045
64	3.902	2.912	3.661	2.614	0.966	0.959	2.174	1.120
65	3.023	2.917	3.097	2.773	2.079	0.888	2.367	1.239
66	2.068	2.967	1.820	3.384	2.581	0.903	2.171	1.192
67	4.266	2.929	3.602	2.713	2.670	0.849	2.064	1.200
68	3.393	2.917	3.726	3.168	3.480	0.987	2.657	1.206
69	1.548	2.922	1.509	3.222	7.879	1.088	2.321	0.969
70	3.504	2.913	3.038	2.494	7.250	0.920	2.093	1.052
71	2.987	2.999	3.813	3.069	5.995	1.079	2.907	1.246
72	1.750	2.992	1.435	3.056	7.004	0.822	2.083	1.225
73	3.035	2.912	2.697	2.407	5.715	0.918	2.224	1.120
74	1.467	2.922	1.487	2.509	3.346	0.964	2.421	1.192
75	3.541	2.984	3.089	2.483	1.015	0.820	2.111	1.243
76	1.376	2.955	1.764	2.513	0.758	1.043	2.651	1.134
77	1.918	2.911	1.687	3.244	5.389	1.034	2.146	0.986
78	2.868	2.942	3.096	2.754	7.647	1.010	2.411	1.163
79	2.355	2.910	2.075	2.883	6.107	0.902	2.214	1.220
80	2.558	2.988	2.423	2.304	1.641	0.880	2.279	1.180
81	2.637	2.941	2.815	3.119	6.169	0.957	2.458	1.228
82	2.946	2.941	3.205	2.524	0.674	1.011	2.539	1.114
83	2.433	2.983	2.478	3.234	1.582	1.037	2.411	1.054
84	2.285	2.935	1.903	2.610	7.282	1.076	2.005	0.869
85	3.398	2.911	2.937	2.488	0.826	0.894	2.022	1.119
86	1.675	2.992	1.747	2.937	0.750	1.010	2.616	1.231
87	4.325	2.947	3.908	2.704	1.889	0.884	2.058	1.161
88	1.272	2.902	1.380	2.395	4.881	0.970	2.382	1.098
89	4.184	2.953	3.861	2.193	4.716	0.932	2.254	1.127
90	3.531	2.969	3.382	2.883	6.227	0.904	2.124	1.179
91	1.220	2.977	1.471	2.812	3.172	1.053	2.759	1.239
92	3.509	2.910	3.612	2.726	2.228	0.994	2.359	1.083
93	2.263	2.957	2.276	2.636	1.896	1.033	2.311	1.030
94	4.064	2.997	3.662	2.542	5.115	0.840	2.033	1.192
95	2.809	2.968	2.479	2.617	5.991	0.792	2.066	1.233
96	1.618	2.908	1.460	3.239	3.339	0.890	2.175	1.151
97	3.426	2.944	3.992	2.718	3.048	1.090	2.703	1.111
98	3.927	2.985	3.745	2.796	4.271	0.895	2.183	1.178
99	1.570	2.969	1.388	2.528	4.145	1.050	2.217	0.948
100	3.412	2.978	3.623	2.807	4.286	0.978	2.303	1.053

Run	Ip	Rmaj	Bphi	Aeff	Ne(0)	Li	q 95	q(0)
101	3.445	2.908	3.560	2.863	2.554	0.937	2.328	1.242
102	2.318	2.944	2.071	2.842	0.984	1.081	2.011	0.884
103	2.379	2.904	2.124	2.643	4.917	1.059	2.038	0.905
104	1.619	2.953	1.775	2.522	3.507	1.064	2.383	1.038
105	3.319	2.972	3.043	3.086	1.129	1.034	2.080	0.895
106	3.549	2.985	3.241	2.441	4.662	0.908	2.008	1.110
107	1.980	2.934	2.352	2.364	7.978	0.983	2.654	1.247
108	3.171	2.982	3.016	2.282	5.399	0.932	2.158	1.157
109	3.827	2.915	3.360	2.471	1.143	0.874	2.178	1.158
110	3.681	2.991	3.538	2.834	2.833	0.962	2.152	1.014
111	3.788	2.959	3.744	2.817	4.491	0.987	2.228	1.086
112	4.195	2.954	3.812	2.125	5.107	0.888	2.190	1.146
113	1.160	2.989	1.082	2.268	5.024	0.886	2.195	1.209
114	3.814	2.980	3.889	2.639	3.351	0.887	2.229	1.181
115	3.194	2.908	3.071	3.086	2.230	0.843	2.129	1.248
116	3.115	2.943	2.913	2.471	2.033	1.007	2.256	1.059
117	2.708	2.950	3.209	2.282	2.971	1.078	2.742	1.139
118	1.325	2.974	1.208	2.802	6.076	0.918	2.138	1.170
119	2.799	2.948	2.779	2.534	2.990	0.898	2.227	1.242
120	2.761	2.957	3.369	2.778	3.477	1.040	2.651	1.119
121	2.757	2.946	2.362	2.521	2.612	0.863	2.158	1.161
122	2.099	2.989	2.291	2.594	6.661	1.053	2.679	1.118
123	1.260	2.918	1.235	2.304	7.620	0.930	2.214	1.111
124	2.723	2.929	2.430	2.763	4.916	0.923	2.161	1.146
125	3.545	2.910	3.343	2.457	0.931	1.071	2.164	0.953
126	1.327	2.988	1.117	2.705	6.280	0.827	2.077	1.235
127	4.359	2.950	3.850	2.756	2.982	1.089	2.050	0.845
128	3.270	2.964	3.430	2.337	7.232	1.055	2.193	0.958
129	1.286	2.997	1.132	2.932	1.449	0.877	2.223	1.215
130	3.928	2.919	3.920	3.033	4.404	0.875	2.220	1.185
131	4.079	2.956	3.487	2.313	6.707	0.873	2.161	1.147
132	2.831	2.953	2.298	3.059	6.839	0.878	2.033	1.154
133	3.296	2.964	3.062	2.458	1.690	0.865	2.147	1.186
134	2.388	2.935	2.296	2.929	2.031	0.809	2.131	1.222
135	3.556	2.915	2.952	2.246	7.960	0.905	2.097	1.161
136	2.018	2.987	2.190	2.217	0.920	0.989	2.333	1.139
137	3.094	2.952	3.023	2.428	5.912	0.909	2.121	1.131
138	1.802	2.918	1.618	2.965	4.667	0.970	2.180	1.005
139	3.860	2.948	3.821	2.816	6.920	1.092	2.305	0.915
140	3.029	2.989	3.865	2.891	1.990	1.067	2.798	1.180
141	2.080	2.956	2.380	2.688	7.567	1.076	2.569	1.083
142	3.525	2.919	3.303	2.074	6.751	1.056	2.259	0.966
143	3.163	2.952	3.521	2.621	7.594	1.059	2.438	1.025
144	3.137	2.981	3.757	2.492	4.183	1.087	2.866	1.230
145	1.461	2.954	1.760	3.025	6.420	0.974	2.751	1.248
146	3.515	2.933	2.919	3.226	2.741	0.895	2.029	1.134
147	2.273	2.987	2.139	2.974	3.922	1.040	2.201	0.955
148	4.073	2.900	3.977	3.163	2.534	0.882	2.199	1.224
149	2.489	2.920	2.692	3.295	5.564	0.973	2.619	1.213
150	4.016	2.996	3.198	2.348	2.692	0.795	2.075	1.214

Table A.2.2 Percentage Gap between the GAE and the Continuum on Axis

Run	n=1	n=2	n=3	n=4	n=5	n=6	n=7
1	10.14	3.71	2.43	2.43	3.29	3.72	4.14
2	5.43	1.15	1.14	2.00	2.86	4.14	5.43
3	8.86	3.29	2.43	3.28	4.14	5.00	5.86
4	5.00	1.14	0.72	1.14	2.00	2.86	4.14
5	0.71	0	0	1.14	2.86	4.57	5.86
6	4.14	0.29	0	0.28	0.72	2.00	2.86
7	0	0	0	0	0	0	0.29
8	3.29	0.29	0	0.28	1.57	2.86	3.72
9	4.57	0.72	0	0	0.71	1.14	2.00
10	0	0	0	0	0	1.14	2.43
11	0.29	0	0	0	0	0	0.28
12	0.72	0	0	0	0.29	1.57	2.43
13	0	0	0	0	0	0	0
14	0	0	0	0	0	0.28	1.14
15	3.71	0.29	0	0.29	1.14	2.00	2.86
16	10.14	4.14	3.29	3.71	4.57	5.43	5.86
17	2.43	0	0	0	0.29	1.14	1.57
18	3.29	0.29	0	0	0.71	1.14	2.00
19	0.29	0	0	0	0	0	0.28
20	5.86	1.57	1.14	1.57	2.86	4.14	5.00
21	7.14	2.00	1.15	1.14	1.57	2.42	2.86
22	7.57	2.00	1.14	1.14	1.57	2.43	2.86
23	0	0	0	0.28	2.00	3.71	5.00
24	1.14	0	0	0	0.29	1.14	2.43
25	6.71	2.00	1.57	2.00	2.86	3.71	4.57
26	7.14	2.00	1.57	2.43	3.29	4.14	4.57
27	4.14	0.29	0.28	1.14	2.43	3.29	4.14
28	2.86	0	0	0	0	0.29	0.71
29	0.71	0	0	0	0	0	0.71
30	0	0	0	0	0	0	0.29
31	0.28	0	0	0	0	0	0.29
32	0.29	0	0	0	0	0	0.28
33	5.00	1.14	0.71	1.57	2.86	4.14	5.43
34	0.29	0	0	0	0	0.28	1.57
35	1.57	0	0	0	0.71	2.00	2.86
36	1.57	0	0	0	0.71	1.57	2.43
37	3.28	0	0	1.14	2.86	4.14	5.43
38	11.00	4.57	3.72	4.14	5.00	5.43	6.28
39	0	0	0	0	0	1.14	2.43
40	2.00	0	0	0	0.28	1.14	2.00
41	0.71	0	0	0	1.14	2.43	3.28
42	4.15	0	0.71	3.72	5.86	7.57	8.86
43	0	0	0	0	0	0	0.72
44	0	0	0	0	0	0	0
45	1.57	0	0	0	1.57	2.86	4.14
46	5.00	1.14	1.57	2.86	4.57	6.29	7.57
47	2.43	0	0	0	0.71	1.57	2.43
48	0	0	0	0	0	0	0
49	1.14	0	0	0	0.28	1.14	2.43
50	2.00	0	0	0	0	1.14	2.00

Run	n=1	n=2	n=3	n=4	n=5	n=6	n=7
101	2.86	0	0	1.14	2.43	4.14	5.43
102	10.14	5.00	5.00	6.72	8.00	9.29	10.14
103	6.71	2.00	1.57	2.00	2.86	3.71	4.57
104	3.72	0.29	0	0	0.71	1.57	2.43
105	11.85	6.29	5.86	7.14	8.43	9.71	10.57
106	0.72	0	0	0	0.28	1.14	2.00
107	1.57	0	0	0	0	0	0.29
108	1.57	0	0	0	0.29	1.14	2.43
109	0	0	0	1.14	3.29	5.00	6.29
110	5.86	1.57	1.14	2.00	3.29	4.57	5.43
111	1.57	0	0	0	0.29	1.14	2.00
112	1.57	0	0	0	0.28	1.14	2.00
113	0	0	0	0	0	0	0
114	0	0	0	0	0	0	0.71
115	0	0	0	0	0.29	1.57	2.86
116	3.29	0	0	1.14	2.86	4.14	5.00
117	4.14	0	0	0	0.71	2.00	2.86
118	0	0	0	0	0	0	0
119	0.29	0	0	0	0.28	1.57	2.86
120	2.86	0	0	0	0	0.29	1.14
121	0.72	0	0	0	1.14	2.43	3.71
122	3.71	0.29	0	0	0	0.72	1.14
123	0.28	0	0	0	0	0	0
124	0	0	0	0	0	0.29	1.14
125	9.29	0	4.57	6.29	8.00	9.29	10.14
126	0	0	0	0	0	0	0.29
127	8.43	3.28	2.86	3.29	4.14	5.00	5.86
128	6.29	1.14	0.29	0.71	1.14	1.57	2.43
129	0	0	0	0	0.71	2.00	3.71
130	2.43	0	0	0	1.14	2.43	3.29
131	3.71	0.71	0	0.29	1.14	2.43	3.29
132	0	0	0	0	0	0.28	1.14
133	0	0	0	0	0	1.14	2.43
134	0.71	0	0	0	1.57	2.86	4.14
135	1.14	0	0	0	0.29	1.14	2.00
136	0	0	0	0	0.71	2.43	3.71
137	0	0	0	0	0	0	0
138	1.14	0	0	0	0	0.71	1.57
139	5.00	0.72	0	0	0.29	0.72	1.57
140	4.14	0	0	0	1.57	2.86	4.14
141	1.14	0	0	0	0	0	0
142	3.29	0	0	0	0	0.71	1.14
143	3.29	0	0	0	0	0	0.72
144	5.43	0.72	0	0.29	1.14	2.43	3.29
145	2.00	0	0	0	0	0	0.28
146	1.57	0	0	1.15	2.86	4.14	5.43
147	9.71	4.57	3.71	4.15	5.43	6.29	7.15
148	0	0	0	0	0.29	2.00	3.29
149	5.86	1.57	0.71	1.14	2.00	2.86	3.71
150	0	0	0	0	0	0.71	1.57

ANNEX 3

Proposal for an Article 14 Contract

GAE Detection for Mass Measurement for Plasma Density Control

Preamble

In view of the interest in obtaining a direct mass measurement in JET D-T plasmas for D/T ratio control, the CRPP would be prepared to perform some numerical simulation work to back up the simple calculations presented so far.

Scope

The scope of the work to be carried out would be two-fold:

1) Use of a cylindrical code, including finite frequency effects in order to identify the dispersion relation of the Global Alfven Eigenmode as a function of the plasma profiles, n_e (r) and q(r). The profiles would be varied in a range to be agreed in advance with JET, and the resonant frequencies calculated for different toroidal mode numbers, 1-7 and for poloidal mode number 0,1,2. This study is effectively a continuation of work carried out previously for TCA but now its in the JET relevant conditions. A copy of the previous work is annexed. The product delivered is to be the frequency separation between the GAE and the minimum of the calculated continuum, for the different profiles chosen. Convolutions of the profiles corresponding to observed parameters, such as ℓ_i and the interferometer chords will be used as "experimental observations", together with the mode frequencies. This will be benchmarked with existing codes at JET.

2) Use of the results obtained in 1) to determine whether the plasma mass can be inferred from the spectrum and other experimentally observable quantities, and with what order of error and different antennae geometries if possible with hardware already existing in JET.

I INTEREST

The interest from JET stems primarily from a desire to know the tritium concentration when injecting T° beams into D^+ discharges. Knowing this would allow us to understand the observed neutron production rate. Experiments with $H^0 \rightarrow D^+$ and $D^0 \rightarrow H^+$ could be used to "calibrate" the T^+ fuelling in simple terms of $10^{19}/m^3$Amp. Since this fuelling efficiency will depend on target density and beam energy, it might be important to conduct very similar non-tritium discharges.

The currently operating TAE system is unsuitable for such mass measurements. The Discrete Alfvén Wave spectrum is less sensitive to the q(r) profile than the TAE spectrum which, in addition, breaks up into a KTAE spectrum in the conditions of most interest, namely with the hottest plasmas. A full theoretical description with the requierd precision to use the KTAE spectrum for mass measurements does not yet exist.

II METHOD AND BIBLIOGRAPHY

The method of estimating the effective mass, defined as $A_{eff} = \Sigma A_i n_i / n_e$ summing over all ion species, was developed on the TCA tokamak [1,2] with a view to measuring either of q(0) or A_{eff}. The method relies on the dispersion relation for shear Alfvén waves, given in the cylindrical approximation by:

$$\omega_{nm}^2 = \frac{B^2}{\mu 0 \rho(r) R^2} \left(n + \frac{m}{q(r)}\right)^2 \left(1 - \frac{\omega^2(r)}{\omega_{ci}^2}\right) \qquad (1)$$

The Discrete Alfvén Waves themselves are characterised by:

$$\omega(n,m) = \left[1 - g(\rho(r), j(r), n, m)\right] * \text{Min}\left(\omega_{nm}(r)\right) \qquad (2)$$

where the offset from the continuum minimum, g, can vary in the range g ~ 0.0 - 0.2. The value of g(ρ(r), j(r), n, m) is obtainable from a toroidal full-wave code such as LION which includes the finite frequency correction automatically. This range of g does not therefore correspond to an uncertainty in ω(n,m), although uncertainties in ρ(r), j(r) will have an effect on the final uncertainty in A_{eff} via the corresponding uncertainty in g. The spectrum obtained assuming f = 0 is shown in Fig. 1, as a function of density.

To calculate this spectrum, we have assumed:

$$n_e(r) = n_e(0) * \left(1 - \frac{r^2}{a^2}\right)^{0.5}$$

$$q(r) = q(0) + (q_a - q_0) * \left(\frac{(r - r_{inv})}{(a - r_{inv})}\right)^2$$

$$r_{inv} = 0.3 * a$$

$$q(r < r_{inv}) = q_0$$

We assumed the following plasma parameters :

B_ϕ	3.4 T
I_p	4 MA
q_0	0.9
R_0	2.9 m
n_{e0}(min)	$3.0 \cdot 10^{19} m^{-3}$
n_{ne0}(max)	$10.0 \cdot 10^{19} m^{-3}$
Impurities	Be, C equal
Z_{eff}	~ 1.5
Main Plasma	D^+, T^+
Injection	H^0, D^0, T^0

New operating conditions can be compared by scaling the DAW frequency by $\left(\frac{B_\phi}{2.8}\right)\left(\frac{n_{e0}}{510^{19}}\right)^{-1/2}$, for example.

Many DAW's can be detected using a wide-band frequency sweep as currently carried out in the TAE diagnostic and A_{eff} can be estimated from the full spectrum. The problems of interpretation are discussed in Section V.

Figure 2 shows a schematic of the diagnostic from power source to data acquisition.

On TCA, about 60W were used with a small poloidal emitting antenna. The wavefield of the DAW was detected by broadband magnetic pick-up coils, mixed with the driving frequency to produce amplitude and phase plots of the DAW spectrum (Fig. 3), as in the JET diagnsotic. This system was used, for example, to measure the effective mass during boronisation experiments which yielded A_{eff} ~ 1.06 [3]. The dynamic behaviour of the effective mass following the influx of cold H^0 into a D^+ discharge was also studied [4].

A second experiment was installed on PETULA in collaboration with CENG. The DAW spectrum was measured using similar techniques to TCA, but the aim of the experiment was to investigate q(0) changes during LHCD sawtooth stabilisation [5]. The TCA generator (< 100W) was re-used. A third experiment was installed by ERM on TEXTOR in collaboration with TCA. The aim was again q(0) measurements, although some impurity injection mass-measurements were performed [6]. The generator used was 400W wideband, from ERM. The DAW's were launched using the ICRF antennae on TEXTOR, but not when they were being powered. Figure 4 shows a rather complicated spectral scan.

The method has been shown to be simple to implement, and the DAW spectrum has never been unexpected, even if it can be quite complex.

The same launching and detection philosophy was followed for the JET TAE active diagnostic, using the saddle coils as antennae, but in the low frequency range 30 - 300 kHz. Software developed at the CRPP for the analysis of the raw JET TAE data runs well for the TAE diagnostic and would be applicable to the DAW diagnostic.

III SCAN RANGE

It is suggested to scan from 0.5 to 4 MHz for the following reasons:

- $|n+m| = 4 - 6$ are visible over the complete density range with D^+
- $|n+m| = 2 - 5$ are visible for H^+

If we can inject higher frequencies than 4 MHz, we would wish to do so, say up to 5 MHz.

As in the case of the TAE diagnostic, the scan range is limited by technical restrictions of resonances at the antenna feeds, in the transmission line and in the antenna itself.

IV REQUIREMENTS

Excitation:

We would inject RF power into one DAW antenna from 0.5 - 4 MHz. The power level is very difficult to estimate, such is the leap from TCA (60 W) and TEXTOR (200 W) to JET, and the uncertainty of the coupling at low n-numbers. A conservative estimate would be to install 2 - 3 kW as for the TAE diagnostic. A more aggressive estimate would assume that advantages of sweep-speed and plasma-surface-area scaling would give 1 kW a good chance. This question will again be resolved by the availability of power sources.

For the design of the launcher, we consider that a target of at least 25 - 30 A would be desirable.

The ICRH antennae cannot be used during their normal operation. Driving by the ICRH beat-frequency appears restrictive. A new antenna would appear to be necessary.

The simplicity of the DAW/TAE launching allows us to conceive of a simple "bent wire" approach. A separate conductor as part of a limiter, proposed by JET, appears attractive. Currents and hence forces in this conductor would be minimal. It needs not to be exposed to the plasma. One end can be grounded to torus earth, requiring only one simple low current low voltage DAW current feed.

Reception

We would use at least 2, and preferably more detectors in reception, sensitive to the frequency range 0.5 - 6 MHz. The amplified signals are mixed with the pilot sweep reference signal to obtain amplitude and phase for each antenna, or for combined antennae, filtering the mixer output as hard as possible to eliminate the effects of Mirnov activity, although the sawtooth response will not be filtered out. The use of several antennae will increase the signal-to-noise ratio, but more importantly allow selection of at least the parity of the toroidal mode number n, reducing the DAW spectrum to two simpler spectra. The overall schema is similar to that for the TAE diagnostic.

The DAW frequency range excludes the use of the present mhd pick-up coils. New coils would need to be conceived and constructed to give a flat response in the range 0.5 - 6 MHz. It would probably be worthwhile to forsee signal combination before mixing, discussed for the TAE diagnostic but not implemented since the parity is defined by the lauching antennas. In the DAW case with one launching antenna the 2 parity combinations could be separated early on in the detection chain.

V LIMITATIONS

Since the experiment would appear to be feasible, we address some issues including the reliability and sensitivity of the result.

1) Toroidicity : The toroidicity in JET is high, so coupling to m = 0, m = 2 will be higher. The spectrum may therefore be richer than previously observed. The sensitivity to major axis shifts will also be greater, introducing an additional error source. Specific commissioning experiments would address this question.

2) n_e profile : The final precision depends upon a good knowledge of the n_e-profile. The relationship (2) is complicated. Nonetheless the results of modelling showed that the A_{eff} weighting is very central (especially from $|n + m| \geq 3$).

3) j-profile : Again relationship (2) depends on the q-profile. As n increases, the q-dependence decreases, showing the importance of a good range of toroidal mode numbers.

4) Frequency estimate : Considered absolutely accurate compared with other uncertainties.

VI EXPLOITATION

Since some problems in V require very detailed experimental results, the approach used on TCA was auto-calibration. A D^+ discharge has an A_{eff} of 2.0, independent of the stripped impurity content. The diagnostic can therefore be calibrated by a sweep through a $D^0 \rightarrow D^+$ discharge with a similar evolution of n_e, β, I_p as a mixed discharge. Asuming that injecting a small addition of H^0 or T^0 will not change $n_e(r)$ (probable), $j(r)$ (possible), β (unknown) would allow us to evaluate the charges in A_{eff} with confidence.

The case of $D^0 \rightarrow H^+$ is not as simple, as the starting A_{eff} is not accurately known. Nonetheless a reasonable estimate of Z_{eff} and n_H will allow a measurement of δn_D assuming impurity content evolution. The more known about n_i in general, the more reliable the estimate of fuelling fraction.

For the $T^0 \rightarrow D^+$ experiment we therefore would need $D^0 \rightarrow D^+$ calibration and $H^0 \rightarrow D^+$ checking for fuelling efficiency.

For the $D^0 \rightarrow H^+$ experiment if considered necessary we would depend on some impurity behaviour knowledge.

VII ORGANISATION

The required equipment is similar to the TAE diagnostics and some might even be shareable :

- RF generator
- 4-Channel mixers
- Broadband amplifiers
- Sweepable pilot generator
- Miscellaneous RF equipment
- Launching antenna + Transmission lines
- Detection probes
- Installation and test of RF generator line
- Tapping 4 RF lines for reception
- System testing
- Acquisition of 8 - 10 channels at < 10 kHz.

In view of its experience at home and abroad as well as on JET using these techniques, the CRPP is interested in collaboration with JET on this measurement on a basis to be discussed in detail.

REFERENCES

[1] G.A. Collins, A.A. Howling, J.B. Lister, Ph. Marmillod, Plasma Phys. and Contr. Fusion **29**, 323 (1987), LRP 294/86 and LRP 196/81.

[2] T. Dudok de Wit, J.B. Lister, B.P. Duval, B. Joye, Ph. Marmillod, Nucl. Fusion **30**, 1493 (1990), LRP 401/90.

[3] Ch. Hollenstein, B.P. Duval, T. Dudok de Wit, B. Joye, H.J. Künzli, P. Oelhafen, R. Zehringer, R. Hauert, E.M. Moser, J. Nucl. Mat. **176**, 343 (1990).

[4] T. Dudok de Wit, B.P. Duval, B. Joye, J.B. Lister, Nucl. Fus. **38**, 359 (1991).

[5] G.A. Collins, A.A. Howling, J.B. Lister, Ph. Marmillod, C. Gormezano, F. Parlange, J.-C. Vallet, D. Van Houtte, Plasma Phys, and Contr. Fusion **29**, 1631 (1987).

[6] P. Descamps, G. Van Wassenhove, R. Koch, A.M. Messiaen, P.E. Vandenplas, J.B. Lister, Ph. Marmillod, Phys. Lett. A **143**, 311 (1990), LRP 391/89.

FIGURE CAPTIONS

Fig. 1 The modelled spectrum of min ($\omega_{min}(r)$) as a function of plasma density, for JET D:T discharges.

Fig. 2 Schematic of the DAW diagnostic.

Fig. 3 Amplitude and phase plots of the DAW spectrum on TCA.

Fig. 4 Spectral scan on TEXTOR

1

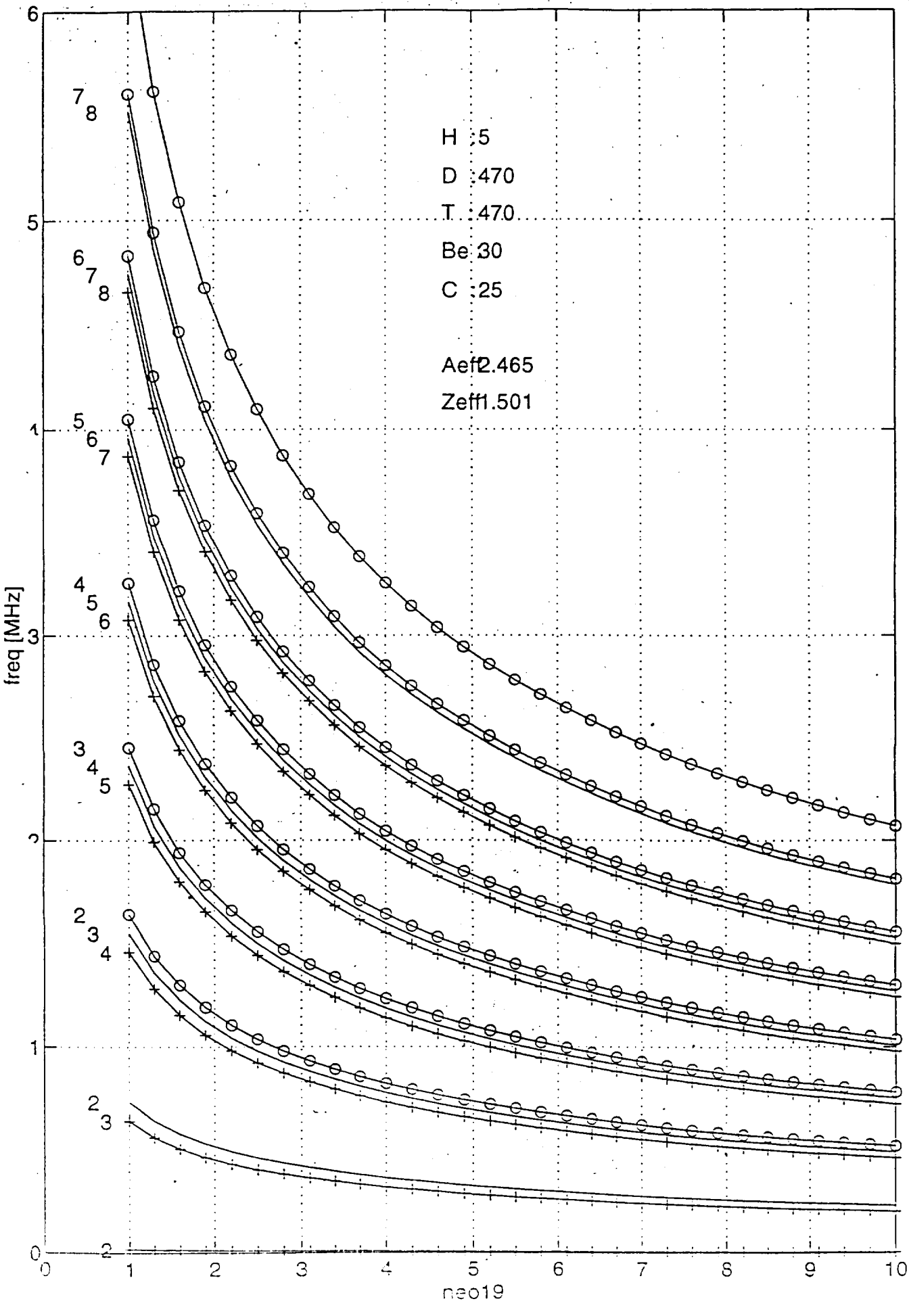
JET DAW for Bphi=3.4, R=2.9, Zeff=1.5, D:T = 47:47
H :5
D :470
T :470
Be :30
C :25
Aeff2.465
Zeff1.501
7 8
6 7 8
5 6 7
4 5 6
3 4 5
2 3 4
2 3
2
freq [MHz]
neo19
0
1
2
3
4
5
6
7
8
9
10

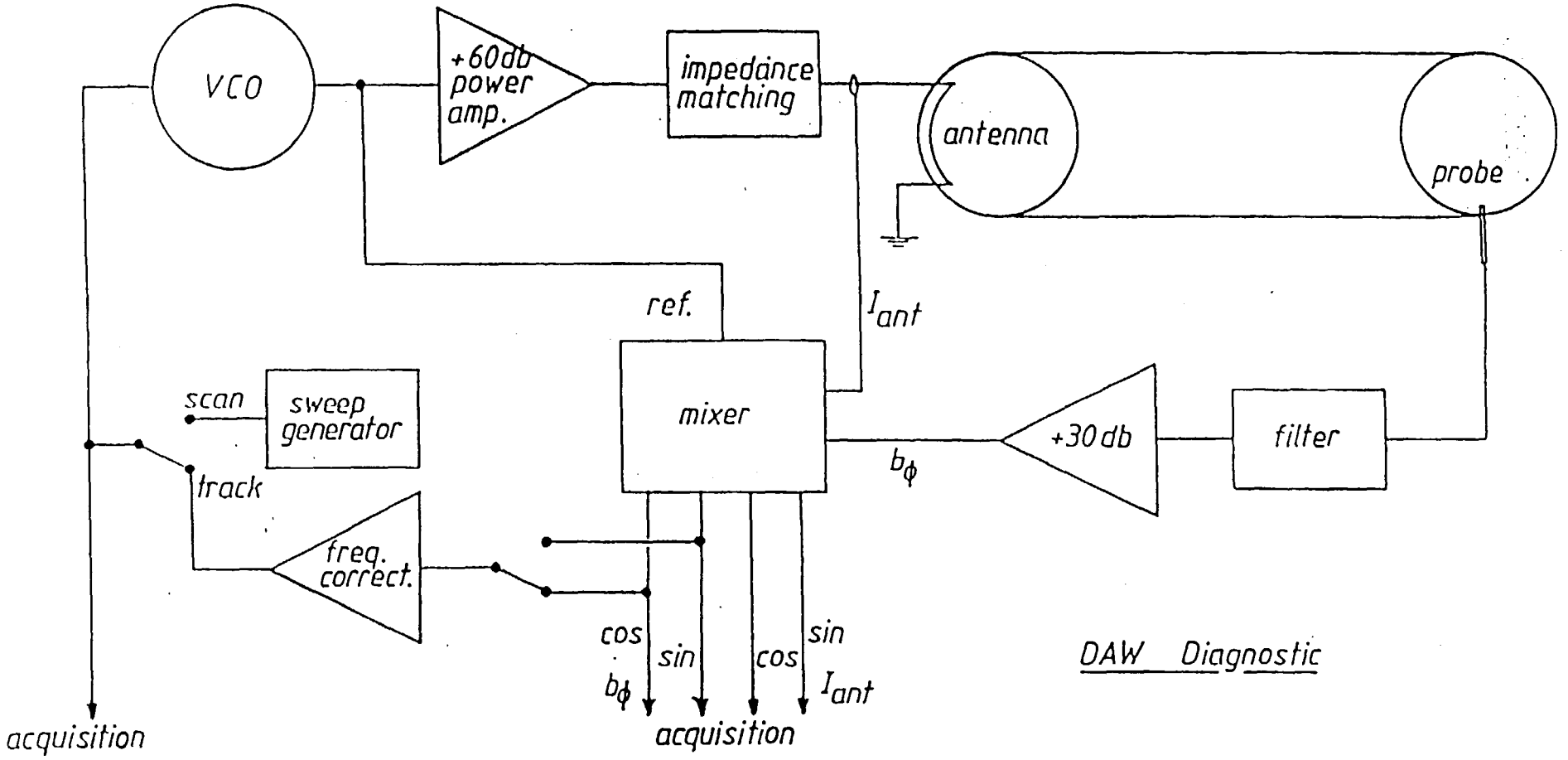
VCO
+60db power amp.
impedance matching
antenna
probe
ref.
I_{ant}
scan
sweep generator
mixer
+30db
filter
track
b_ϕ
freq. correct.
cos
sin
cos
sin
b_ϕ
I_{ant}
acquisition
acquisition
DAW Diagnostic

FIG. 2

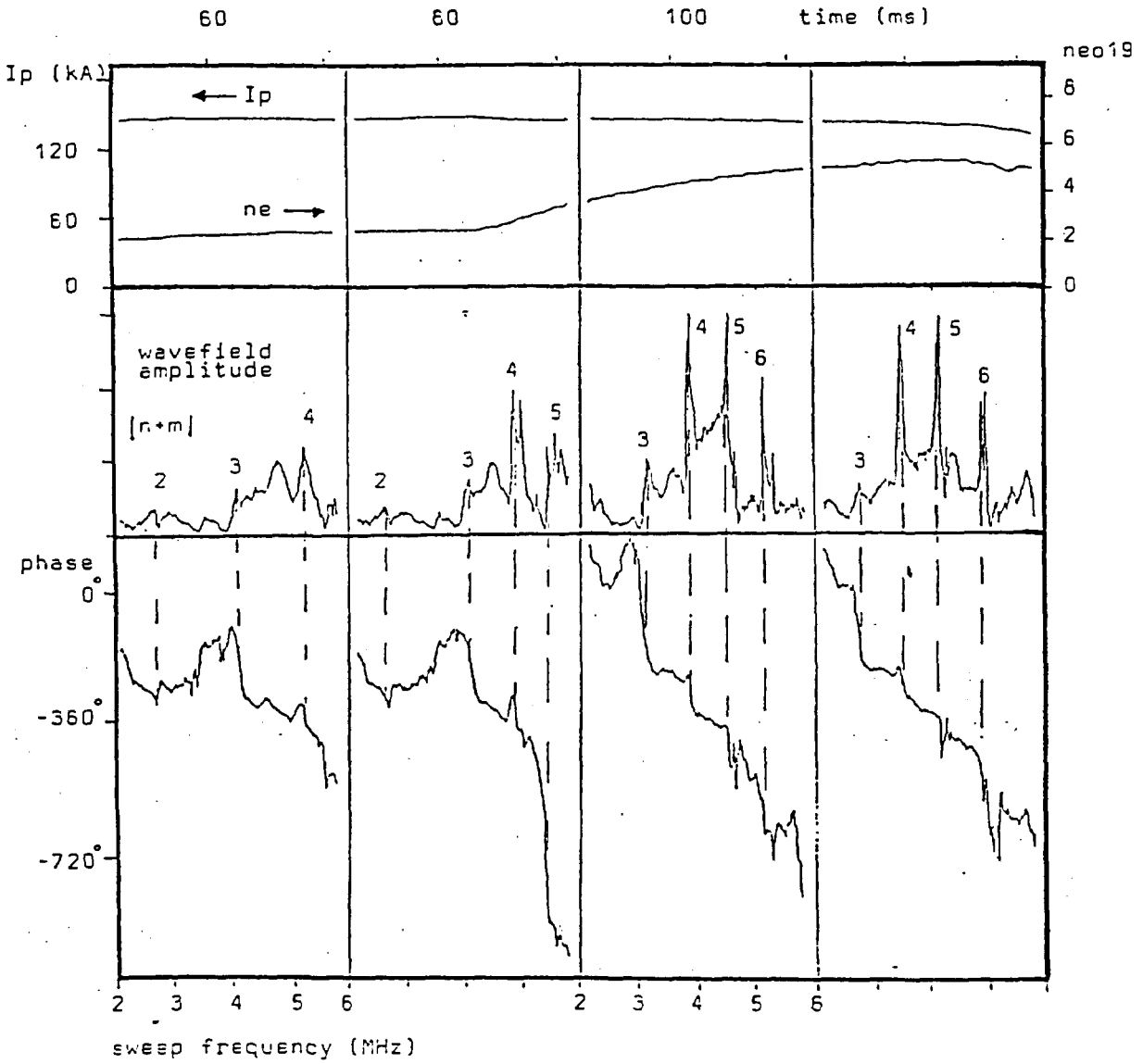
60
60
100
time (ms)
Ip (kA)
Ip
120
ne
60
0
neo19
8
6
4
2
0
wavefield
amplitude
[n+m]
2
3
4
5
6
phase
0°
-360°
-720°
2 3 4 5 6
2 3 4 5 6
sweep frequency (MHz)

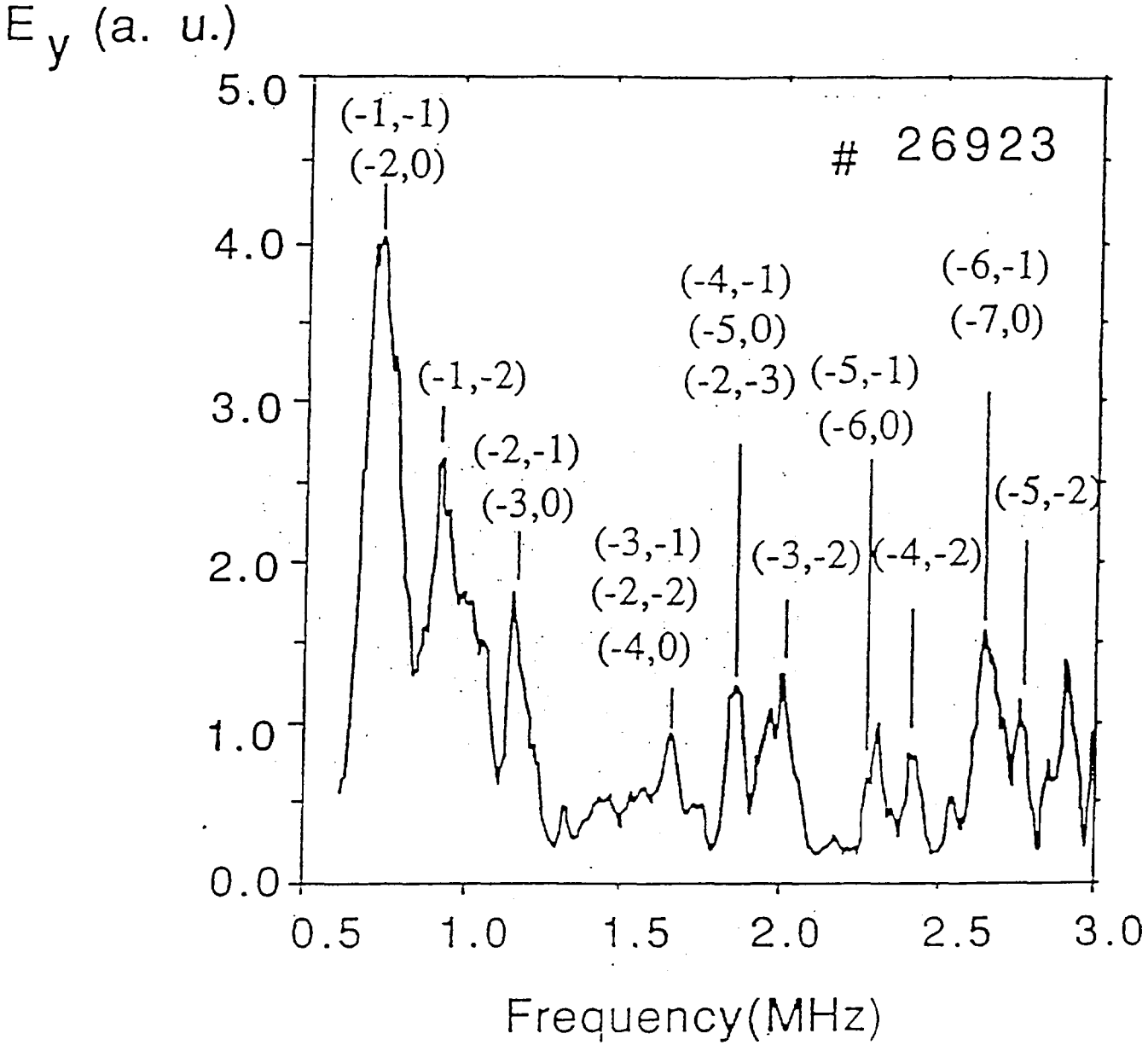
E y (a. u.)
5.0
4.0
3.0
2.0
1.0
0.0
0.5
1.0
1.5
2.0
2.5
3.0
Frequency(MHz)
# 26923
(-1,-1)
(-2,0)
(-1,-2)
(-2,-1)
(-3,0)
(-3,-1)
(-2,-2)
(-4,0)
(-4,-1)
(-5,0)
(-2,-3)
(-3,-2)
(-5,-1)
(-6,0)
(-4,-2)
(-6,-1)
(-7,0)
(-5,-2)

FIG. 1

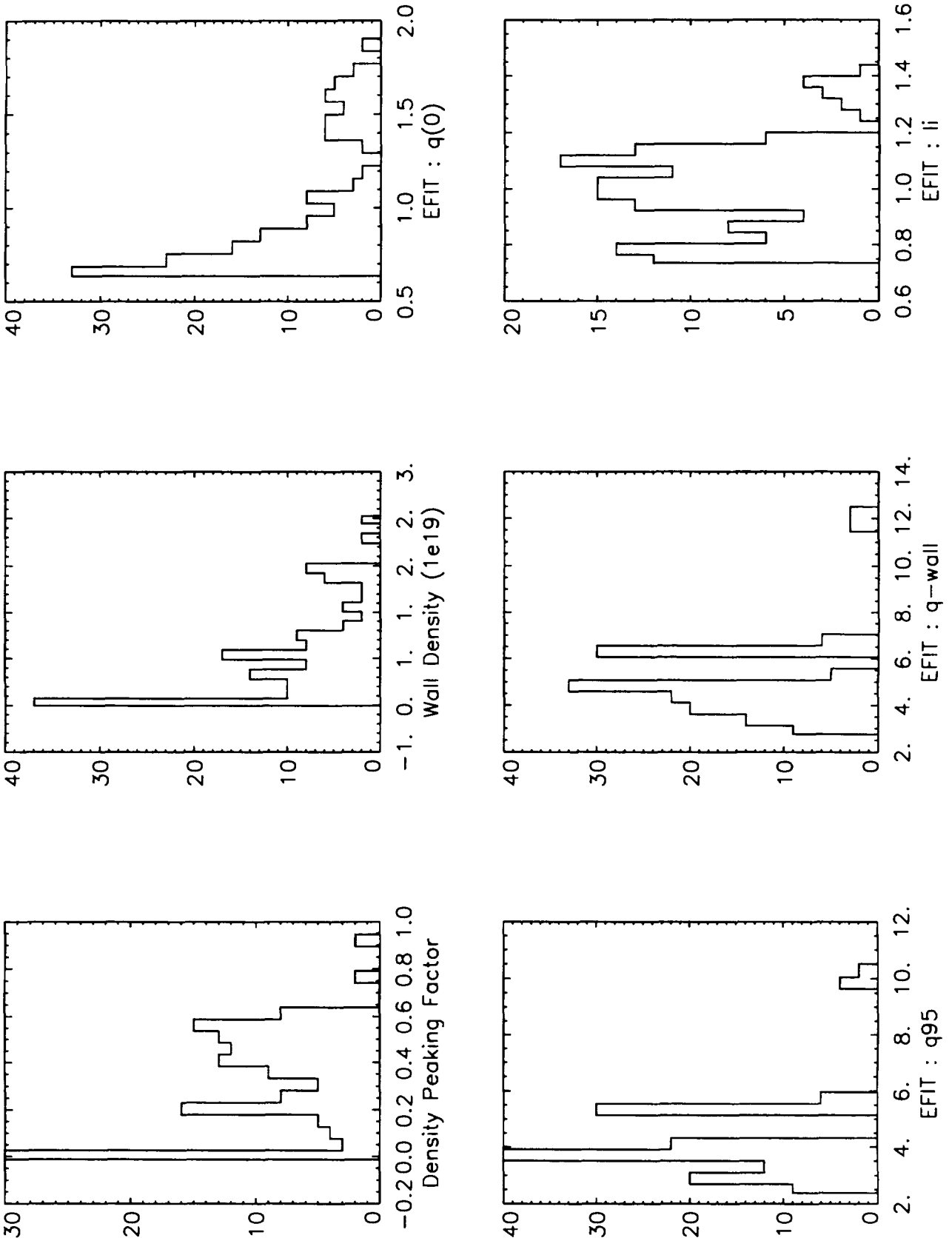

3.1.1(a) Distributions of parameters in the JET database.

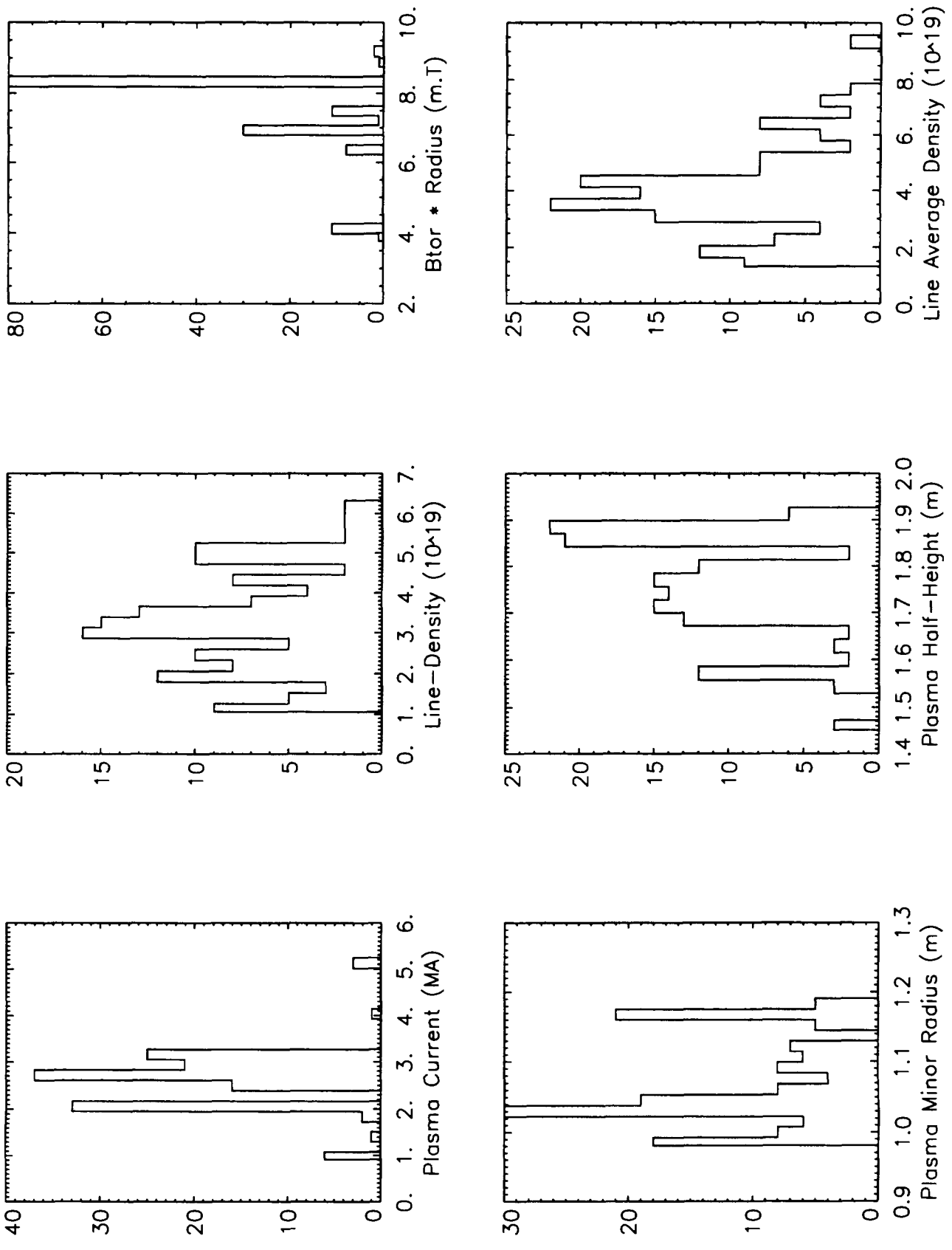

3.1.1(b) Distributions of parameters in the JET database.

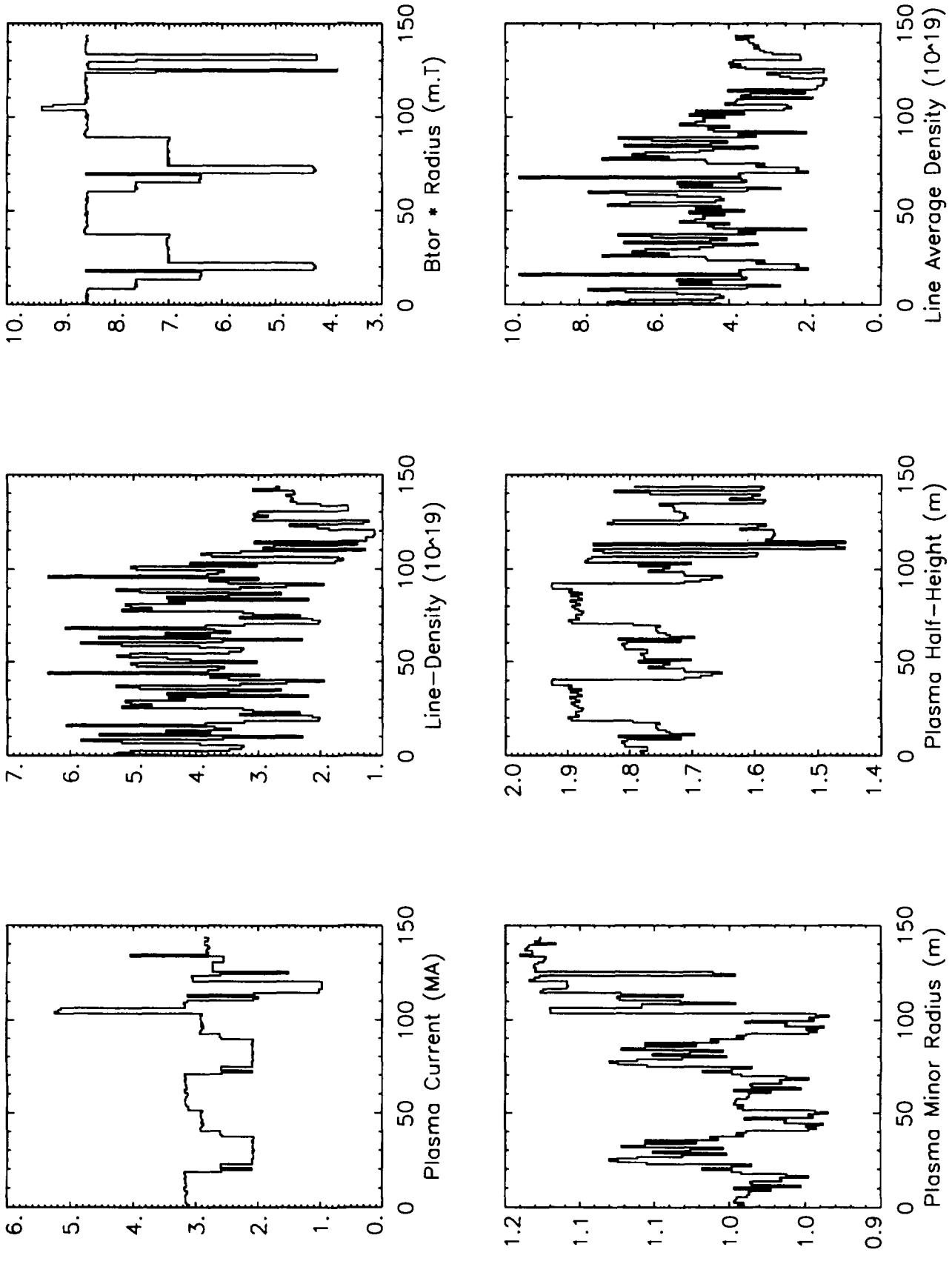

3.2.1(a) Distributions of the individual parameters chosen to be representative of JET data on a discharge by discharge basis.

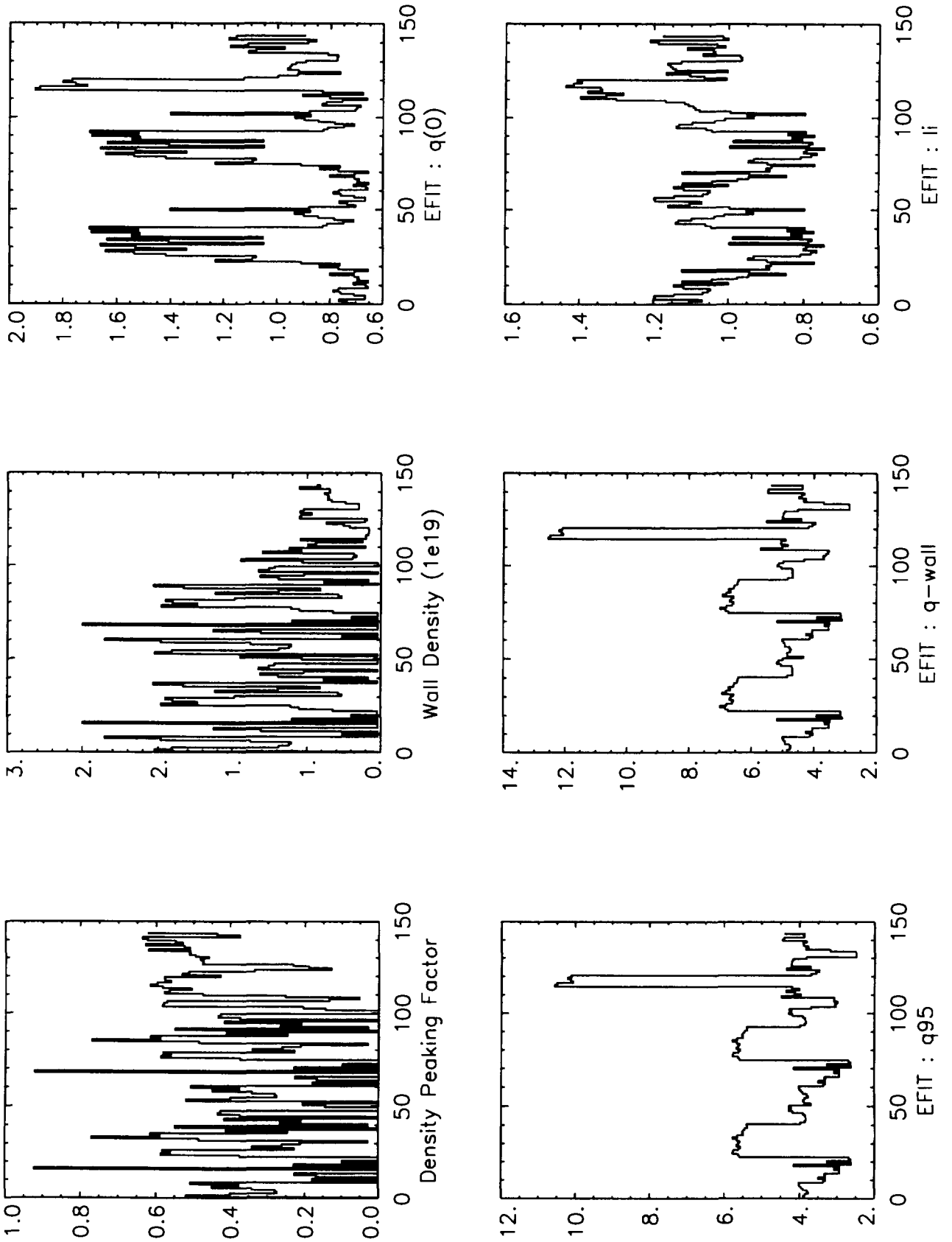

3.2.1(b) Distributions of the individual parameters chosen to be representative of JET data on a discharge by discharge basis.

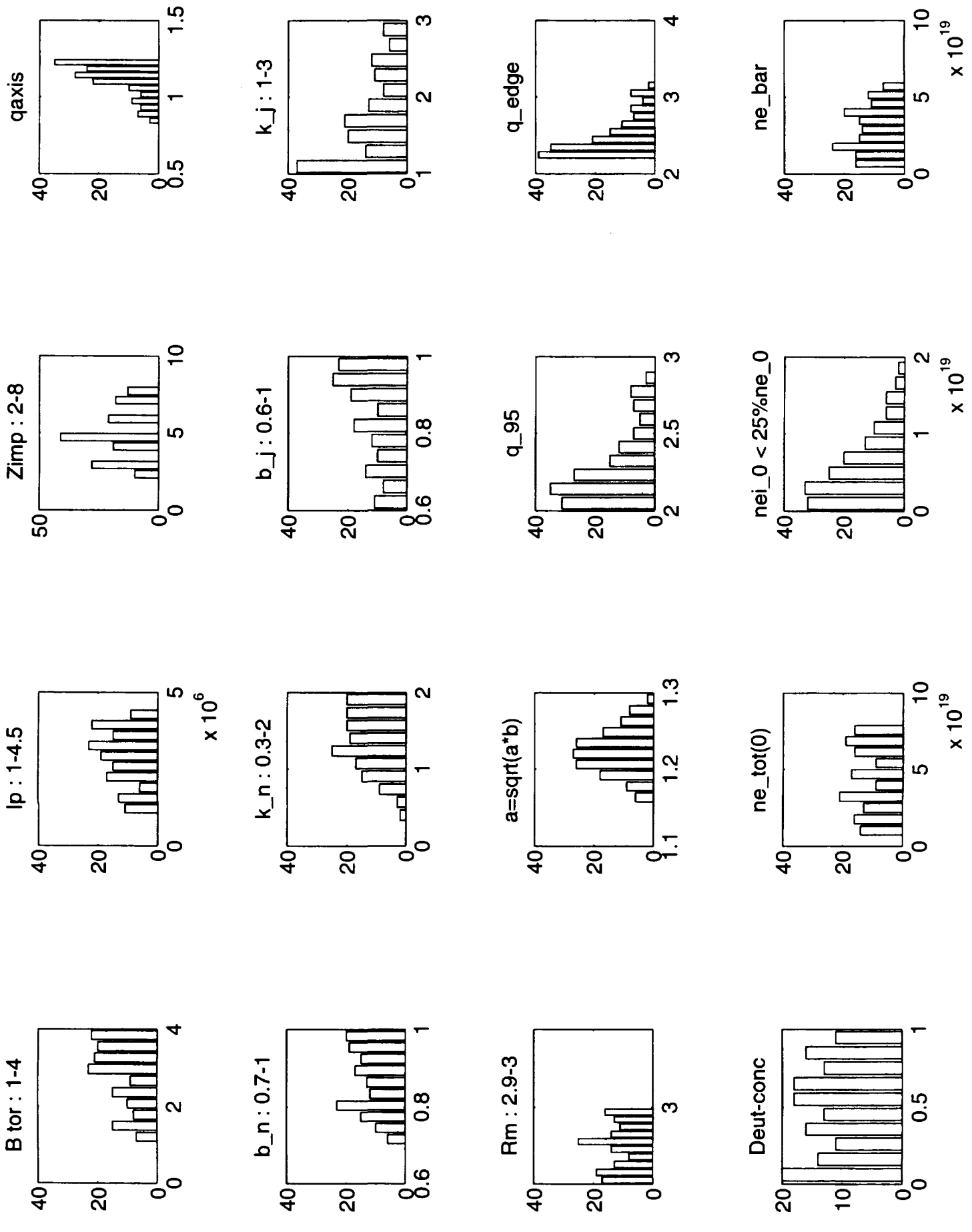

3.2.2(a) Distributions of the individual parameters chosen to be representative of JET data, histogrammed.

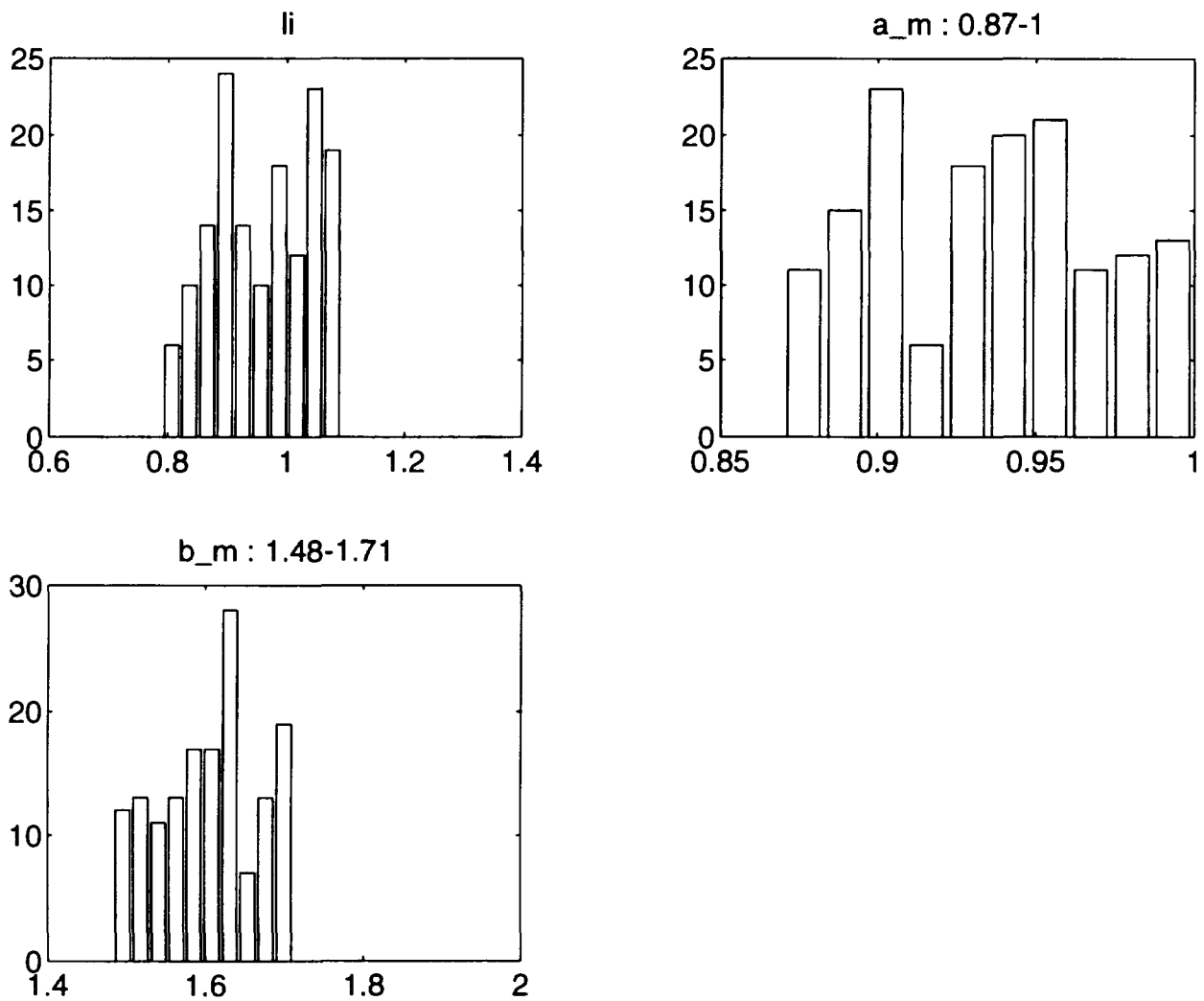

3.2.2(b) Distributions of the individual parameters chosen to be representative of JET data, histogrammed.

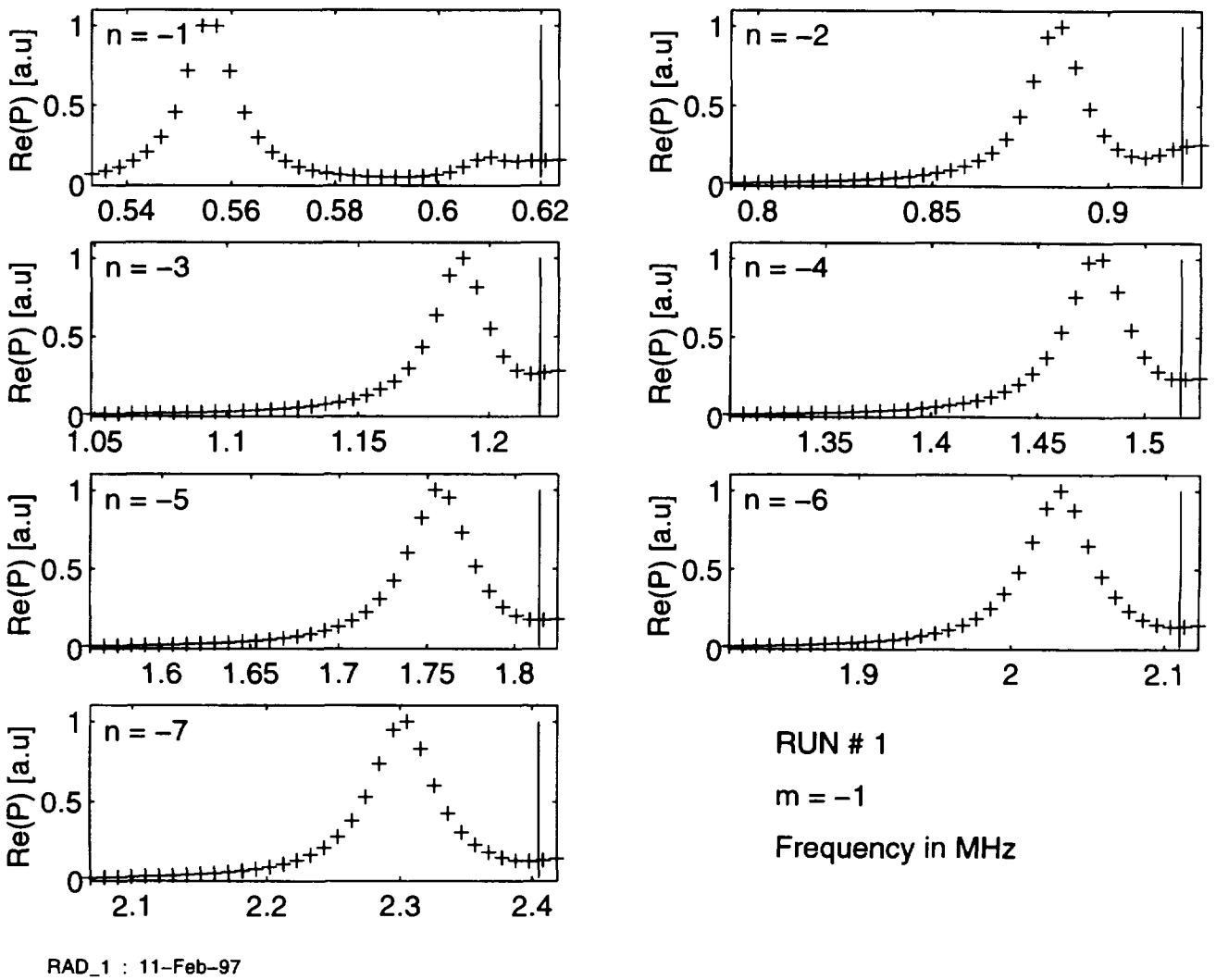

3.3.1(a) Spectral scan over the test run # 1 listed in Table 3.3.1.

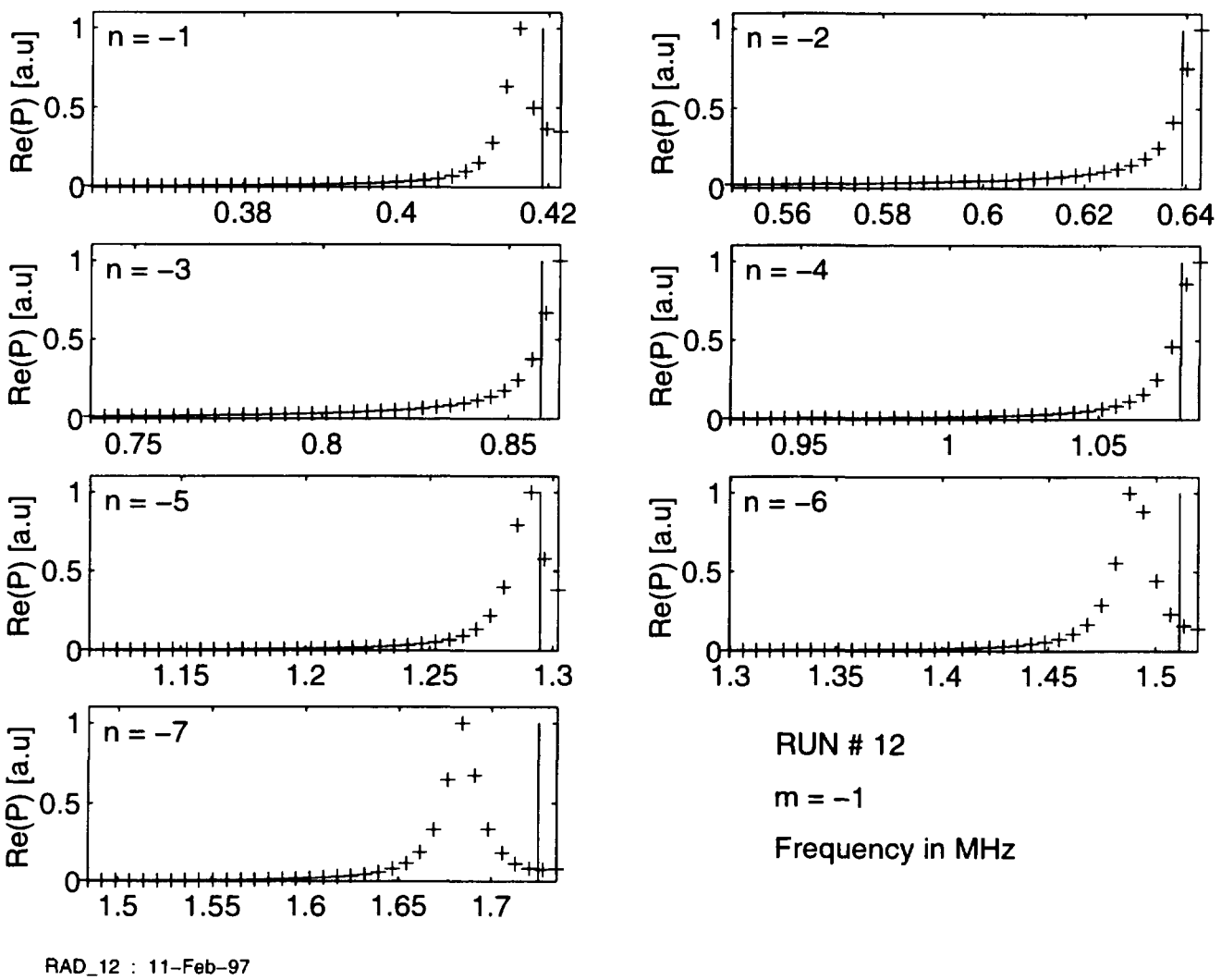

3.3.1(b) Spectral scan over the test run # 12 listed in Table 3.3.1.

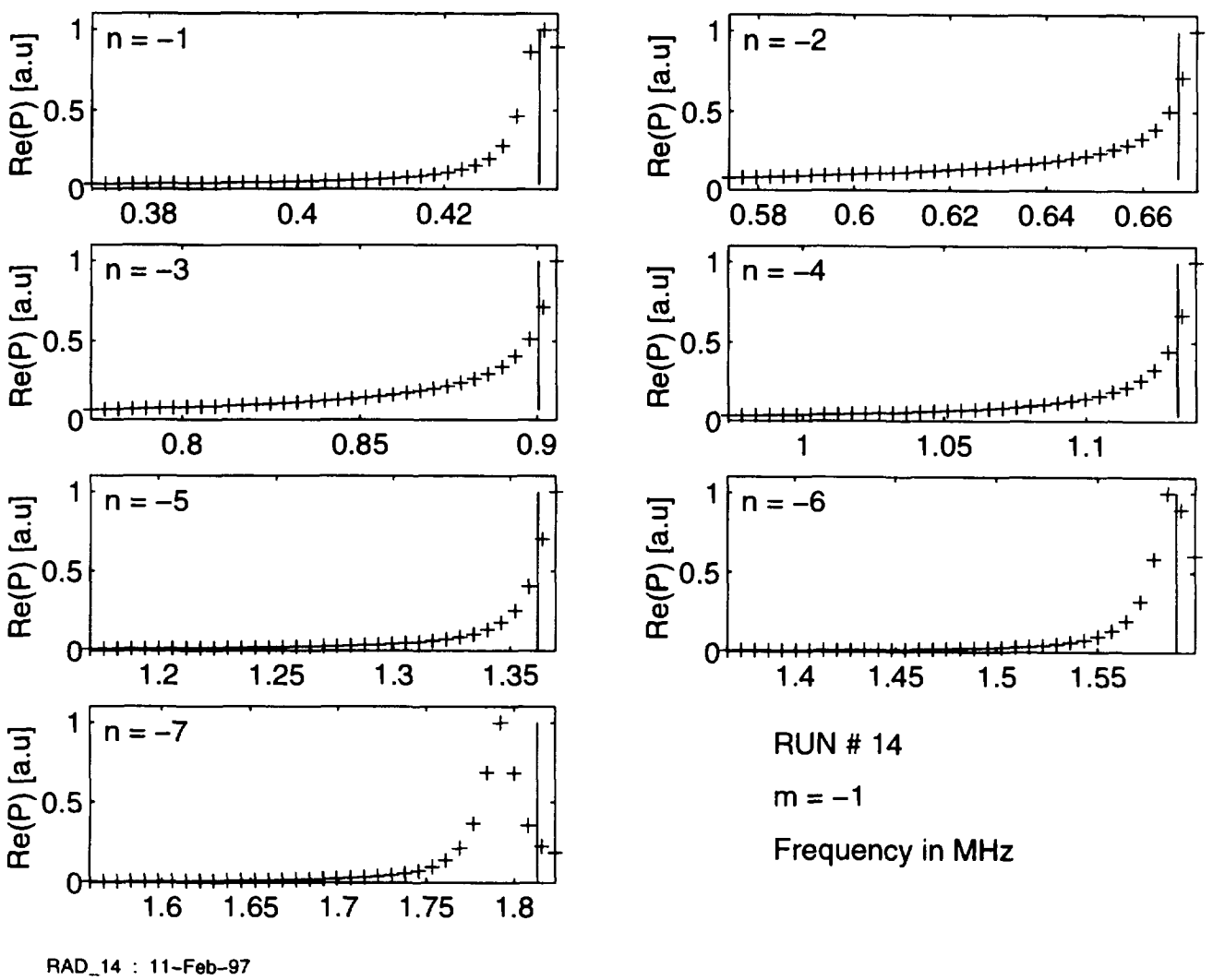

3.3.1(c) Spectral scan over the test run # 14 listed in Table 3.3.1.

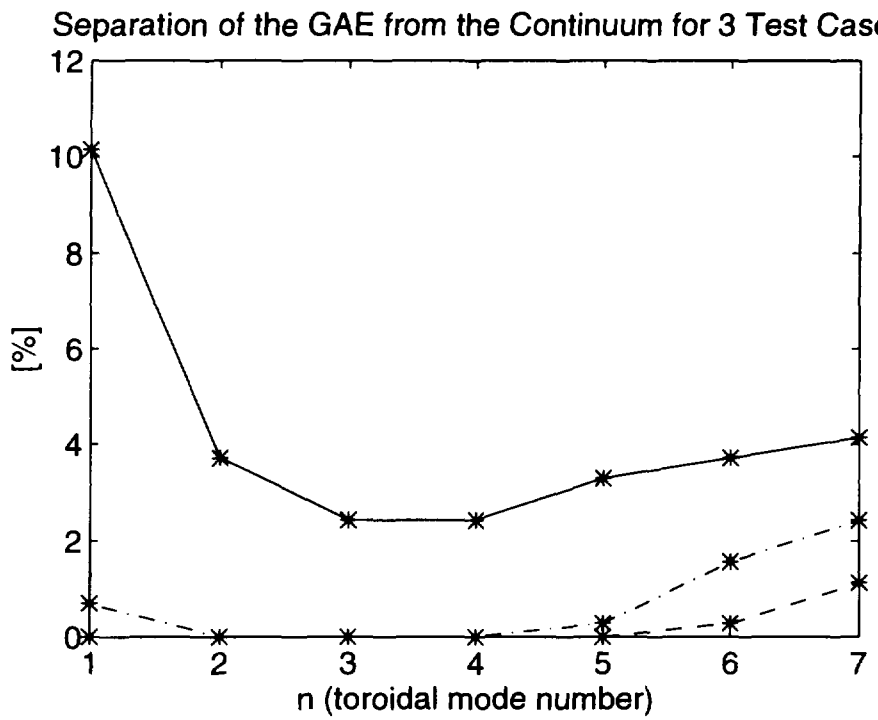

GAE_GAP : 10-Feb-97

4.1.1 GAE separation as a function of toroidal mode number for the 3 test cases. The solid line is case No 1, the dashed line is case No 14 and the dot-dashed line is case No 12.

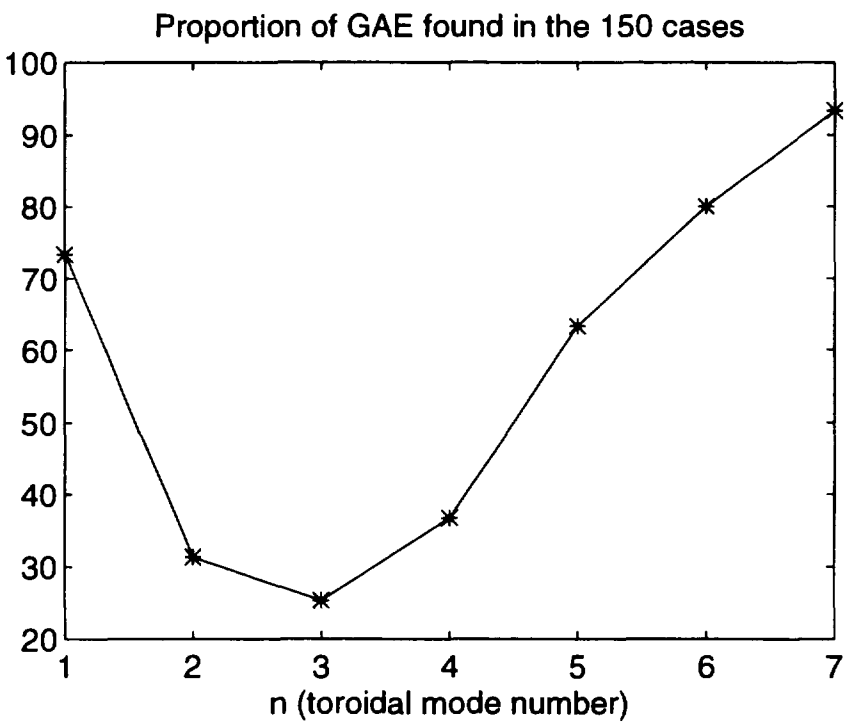

GAE_PROP : 10-Feb-97

4.1.2 Fraction of GAEs found in 150 test runs, as a function of the toroidal mode number.

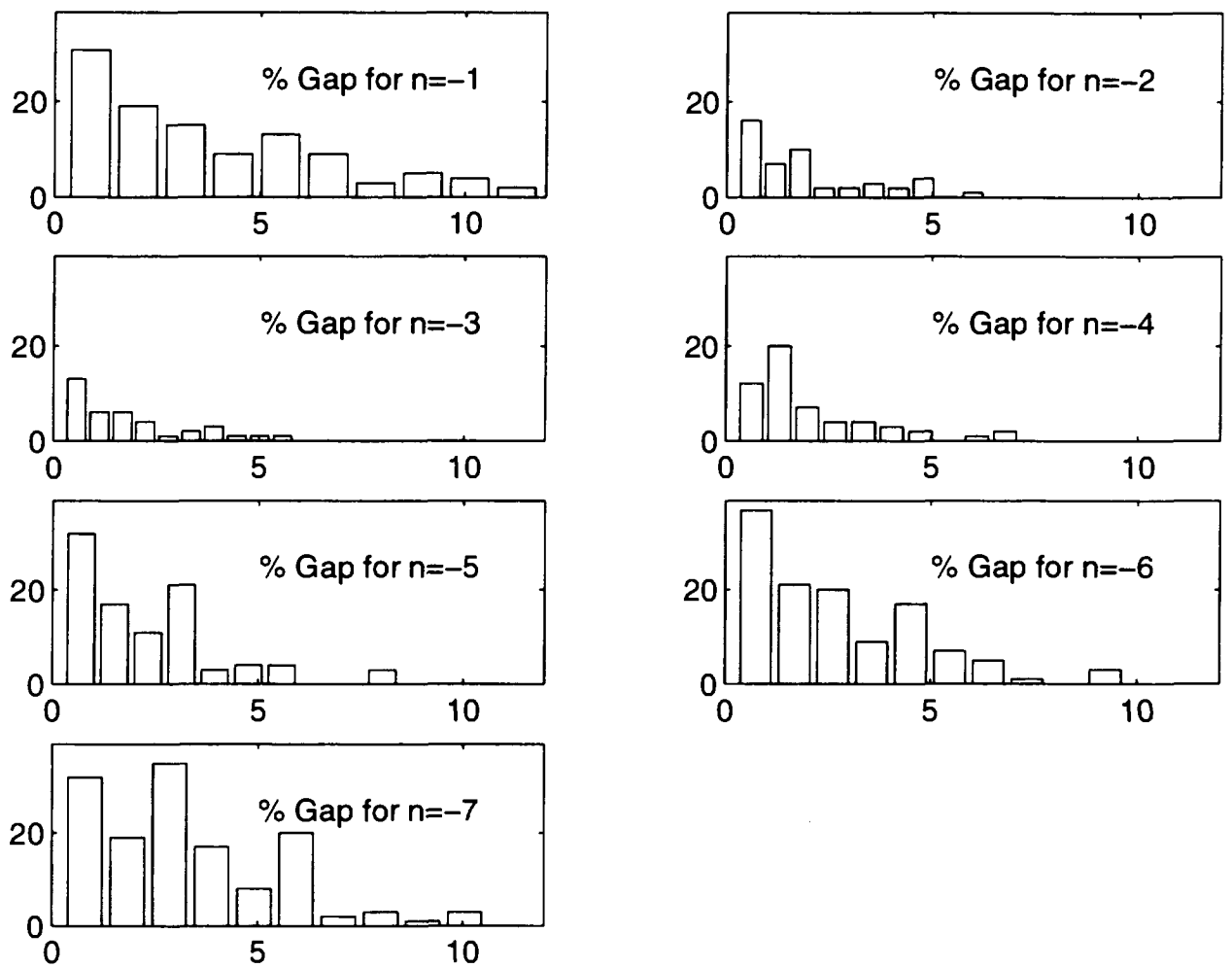

4.1.3 Spread of $\delta\omega/\omega$ for different toroidal mode numbers.

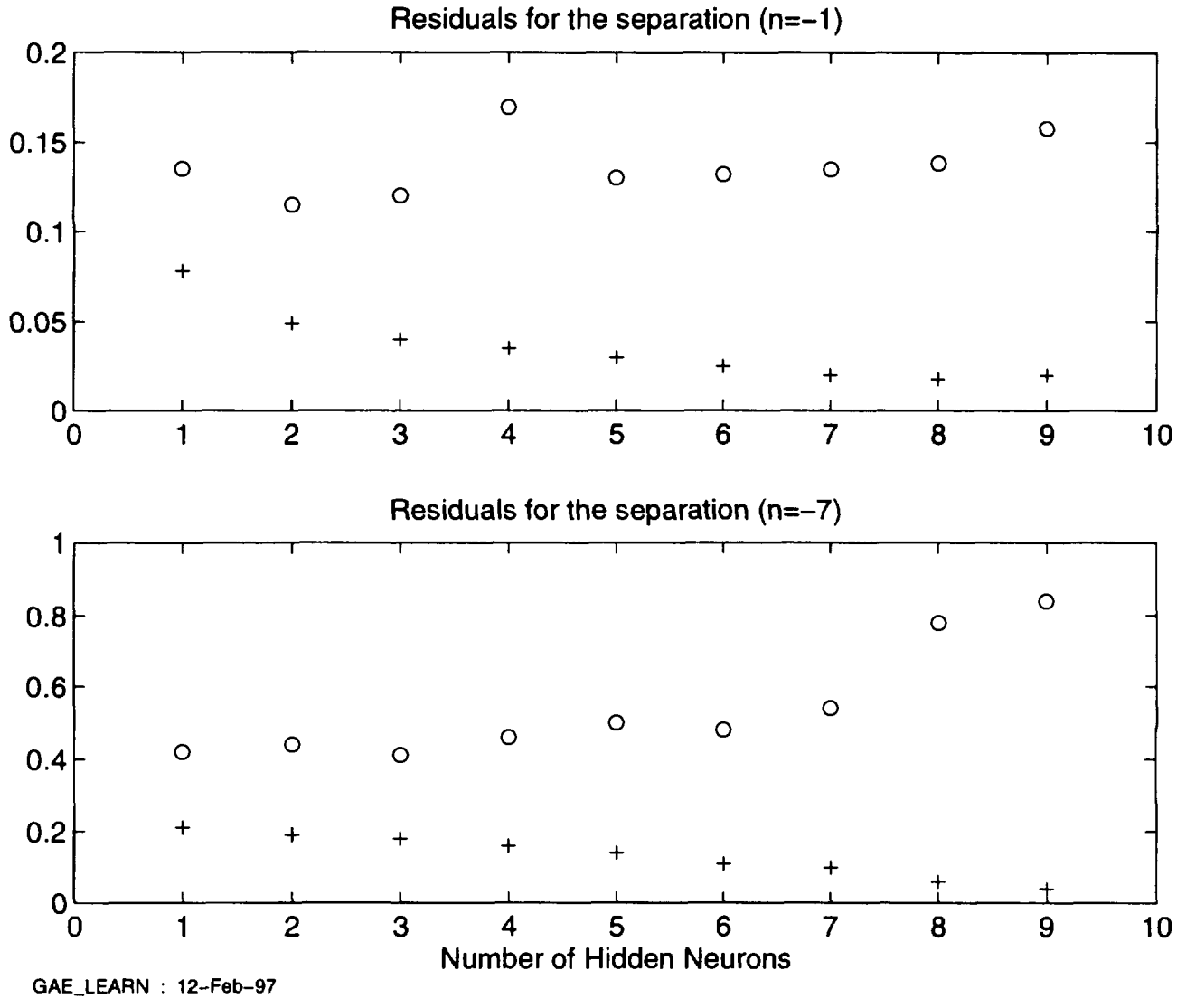

4.2.1 RMS residual when fitting GAE separation to the imposed plasma parameters. Crosses are fitted population, open circles are the test population.

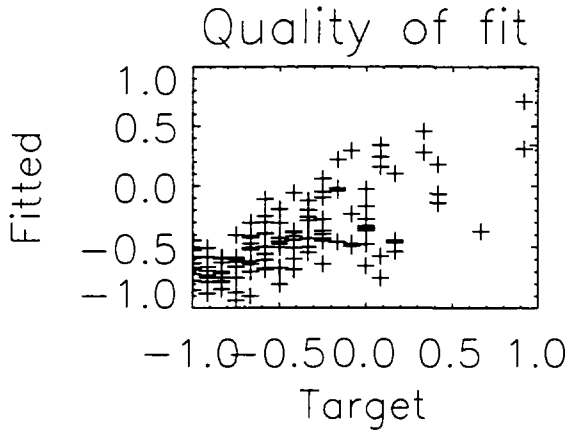

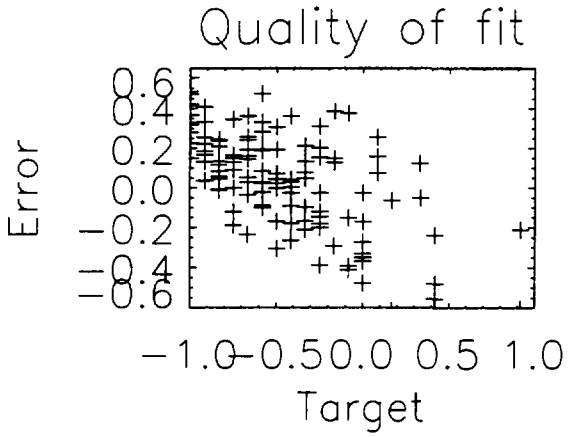

algo : GAR
problem : GAE GAP FOR N = −7
output nr: 0
name : Gap
from : 0
to : 139
max error : 0.554498
min error : −1.04003
mean error 2.61945e−05
rms error : 0.304024
%FS error 15.2012
Scale 5.14400
Min/Max 0.28241910.5704
26−Mar−1997 11:48:13.00

4.2.2 Representation of the residuals as a function of the target values for n = -7 and 4 hidden elements.

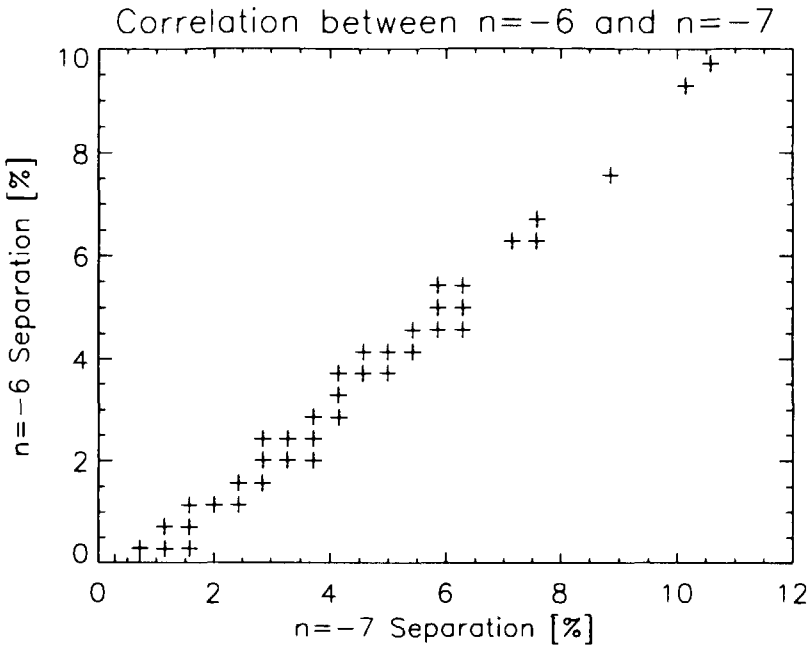

4.2.3 Correlation between the $\delta\omega/\omega$ [%] obtained for n = -6 and n = -7 GAE.

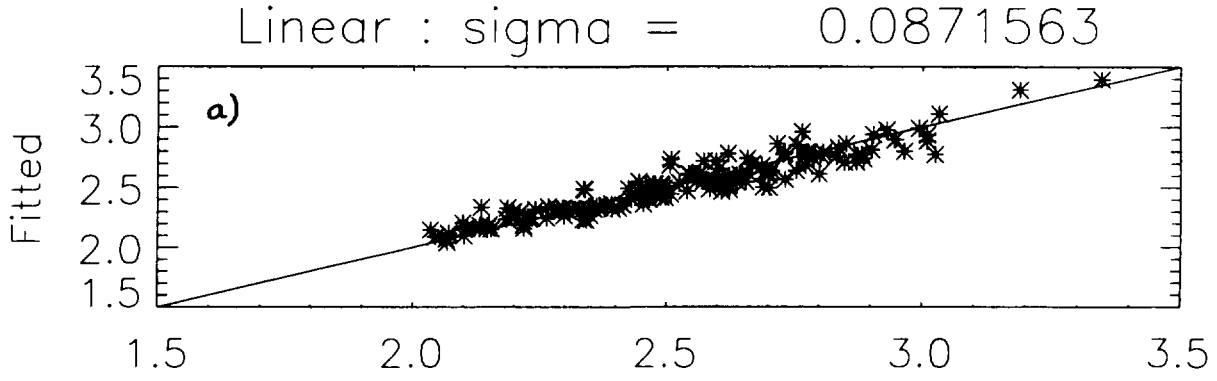

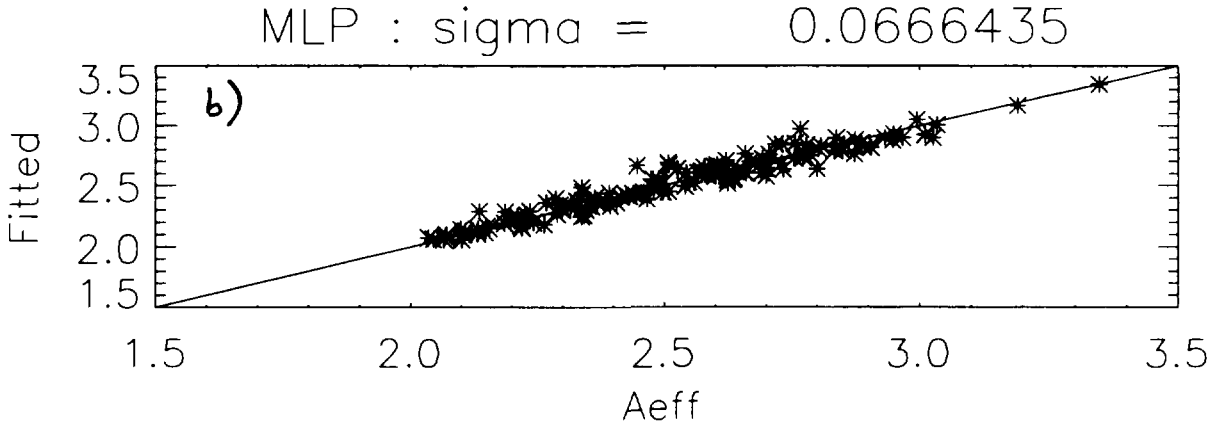

4.3.1(a) The A_{eff} residuals for a linear fit.

4.3.1(b) The A_{eff} residuals for an MLP fit.

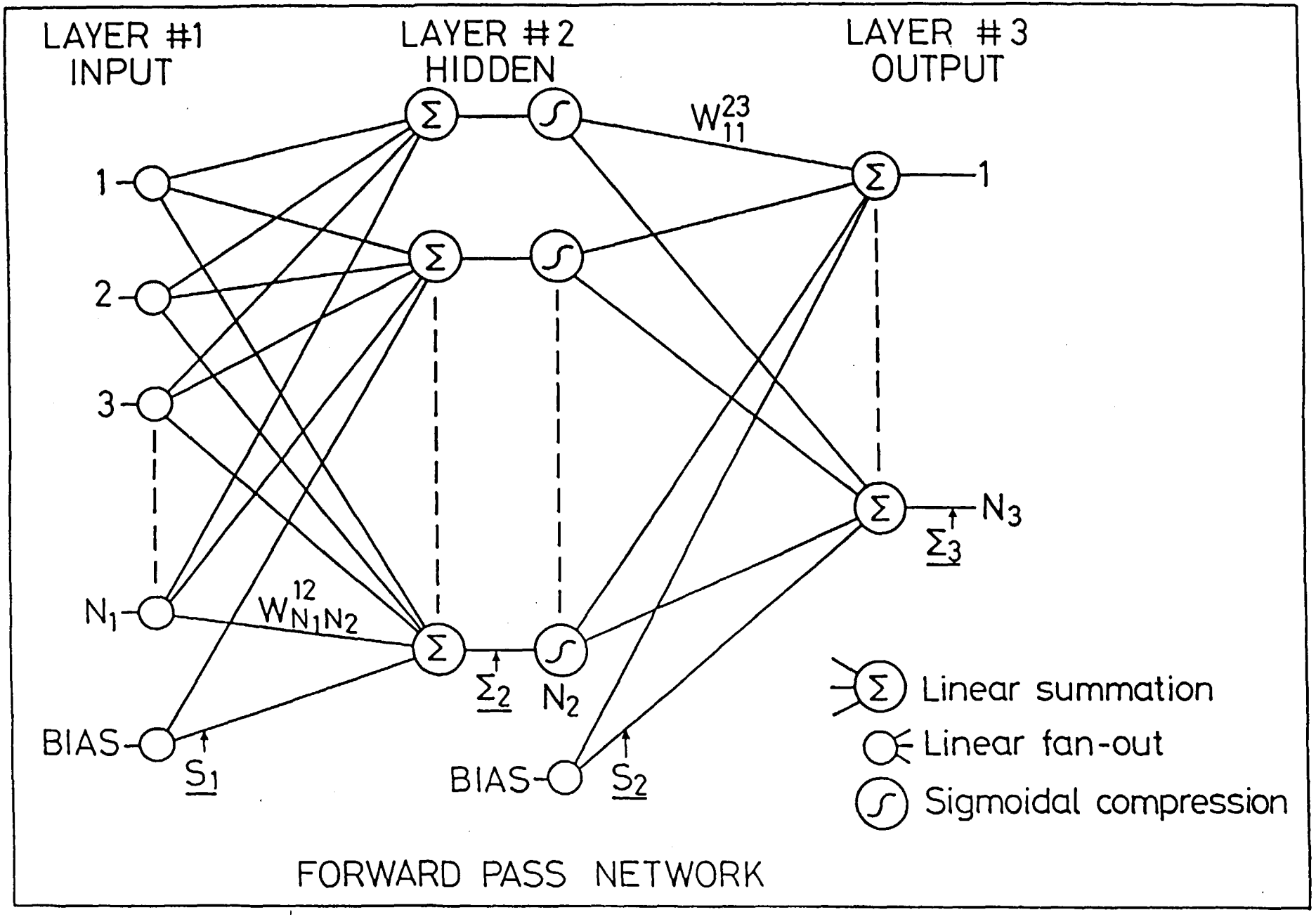

A.2.1. Schematic of the Multi-Layer Perceptron.